Impact of bi-directional loading on the seismic performance of C-shaped piers of core walls

Anahid A. Behrouzi [a,*], Andrew W. Mock [b], Dawn E. Lehman [c], Laura N. Lowes [c], Daniel A. Kuchma [d]

[a] Architectural Engineering, California Polytechnic State University, San Luis Obispo, CA, United States
[b] Exponent, Warrenville, IL, United States
[c] Civil and Environmental Engineering, University of Washington, Seattle, WA, United States
[d] Civil and Environmental Engineering, Tufts University, Medford, MA, United States

ARTICLE INFO

Keywords:
Reinforced concrete
Core wall
C-shaped walls
Large-scale laboratory tests
Bi-directional loading
Seismic performance

ABSTRACT

Reinforced concrete structural walls are commonly used as the primary lateral load resisting system in modern buildings constructed in high seismic regions. Most walls in high-rise buildings are C-shaped to accommodate elevators or other architectural features. C-shaped walls have complex loading and response including: (1) symmetric response in the direction of the web, (2) asymmetric response in the direction of the flange and (3) high compression and shear demands when used as a pier in a coupled-wall configuration. A research study was conducted on C-shaped walls tested under (1) uni-directional and (2) bi-directional loading of an isolated walls and (3) bi-directional loading of a c-shaped pier in a coupled wall system. Each of the walls failed in flexure with strength loss resulting from low-cycle fatigue of the boundary element longitudinal reinforcement with buckling followed by fracture. The damage progression was as follows: (1) cracking at the wall-foundation interface, (2) concrete spalling in the web, (3) buckling and fracture of web reinforcement, (4) spalling in the flanges, (5) buckling and fracture of the bars in the boundary elements. Concrete spalling and steel bar damage occurred at lower strong-axis drift levels for the bi-directionally loaded, resulting in lower drift capacities for these loading protocols. However, for the strong-axis direction, bi-directional loading does not reduce flexural or shear effective stiffness values suggesting that current values are appropriate for design and evaluation of buildings with c-shaped walls.

1. Introduction

Reinforced concrete (RC) structural walls are used frequently as the lateral load resisting system for mid- and high-rise buildings in seismic regions. Slender RC walls are relatively stiff under service-level loading and are designed to suppress shear failure and exhibit ductile flexural response under severe earthquake loading [1]. This experimental study investigates C-shaped walls which are commonly used as isolated or piers in coupled walls where the configuration encloses a service, elevator, or stairwell core [2]. C-shaped core wall systems enhance structural performance by providing bi-directional strength and stiffness while allowing for architectural flexibility in a building floor plan [3]. Additionally, non-planar walls with properly detailed boundary elements can yield a significant savings in reinforcement quantity and simplification of construction, thus leading to notable time and money savings [4]. For these reasons, there is widespread reliance on flanged (L, T, and C) RC walls by practicing engineers.

The research presented in this paper represents the final phase of a multi-year effort which also includes large-scale laboratory experiments of planar and coupled walls [5,6]. Three nominally identical C-shaped walls were tested at the Newmark Structural Engineering Laboratory (NSEL) "Multi-Axial Full-Scale Sub-Structured Testing and Simulation" (MUST-SIM) facility at the University of Illinois at Urbana-Champaign to examine the effects of uni- and bi-directional loading on an isolated wall, as well as bi-directional loading with simulated coupling action on a wall pier in a core wall system. The primary objective of this study was to generate high fidelity response and damage data for C-shaped walls with detailing based on both modern codes and a survey of wall designs in recently constructed West Coast mid- and high-rise buildings. These comprehensive experimental datasets were made publicly available to inform researchers and practitioners in simulating non-planar walls to

* Corresponding author at: 1 Grand Ave, San Luis Obispo, CA 93407, United States
E-mail address: behrouzi@calpoly.edu (A.A. Behrouzi).

Nomenclature

b	width of boundary element
f_c'	concrete compressive strength
f_r	concrete rupture strength
f_u	steel ultimate strength
f_y	steel yield strength
h_{10}	height of 10-story prototype specimen
h_{eff}	effective wall height based on ASCE 7 Equivalent Lateral Force (ELF) Procedure
h_s	experimental specimen height
l_f	flange length
l_w	wall length
t_f	flange thickness
t_w	wall thickness
A_{eff}	effective area of wall
A_{cv}	shear area of wall
A_g	gross area of wall
E_c	elastic modulus of concrete
G_c	shear modulus of concrete
I_{eff}	effective moment of inertia of wall
I_g	gross moment of inertia of wall
M_b	experimental base moment
M_{cr}	expected cracking moment, considers impact of axial load
M_{max}	maximum experimental base moment
M_n	nominal moment strength, calculated per ACI 318
M_u	ultimate moment demand used in design of specimens
V_b	experimental base shear
V_{eff}	effective shear demand, based on ASCE 7 ELF Procedure
V_i	shear demand for story level *i*, based on ASCE 7 ELF Procedure
V_{max}	maximum experimental base shear
V_n	nominal shear strength, calculated per ACI 318
V_u	ultimate shear demand used in design of specimens
ε_{cu}	concrete ultimate strain
ε_{sh}	steel strain hardening strain
ε_u	steel ultimate strain
ε_y	steel yield strain
ϕ	strength reduction factor per ACI 318 (0.75 for shear, 0.9 for flexure)
$\rho_{BE,con}$	boundary element confinement reinforcement ratio
$\rho_{BE,l}$	boundary element longitudinal reinforcement ratio
$\rho_{web,h}$	web horizontal reinforcement ratio
$\rho_{web,l}$	web longitudinal reinforcement ratio

more accurately predict demands and damage [7–9].

2. Previous experimental research on C- and U-shaped walls

The results of previous tests involving slender C- and U-shaped wall specimens were reviewed to understand how this wall type performs and to establish previously investigated parameters. A total of seven large-scale test specimens from three test programs [2,10,11] were identified. Table 1 presents a comparison of the loading, geometry, reinforcement ratios, and wall-to-foundation connection of selected prior tests to the C-shaped wall tests [12] that are the subject of this paper.

Prior tests indicate the following differences between nonplanar and rectangular wall response:

- Thinner planar walls are vulnerable to compression-controlled failure due to appreciable spalling in unconfined regions that reduce section capacity [2,10]. However, thin walls with nonplanar geometries are often able to achieve moderate ductility by lateral load transfer to well-detailed boundary elements that are engaged through framing action [2].
- Shear contribution to overall deformation tends to be higher for nonplanar walls compared to rectangular walls. Therefore, shear and shear sliding are of more concern for these walls [2].

For nonplanar walls, experimental observations indicate that compared to uni-directional loading, bi-directional loading results in:

- Reduced drift capacity in both strong- and weak-axis loading directions as well as more rapid strength loss [2,11].
- Shear primarily carried by the compression region (flange) rather than the entire shear area parallel to the loading direction, as typically assumed in design [11].

Examination of Table 1 indicates that the current tests has similarities in terms of geometry and reinforcement to Sittipunt & Wood [10], but Lowes [12] adds in the important study parameters of bi-directional loading (CW2) and varying axial load (CW3) demands on a C-shaped

Table 1
Summary of C-shaped Wall test specimens from previous and this research studies.

Reference	Name	*Loading Direction*			*Geometry*			Avg reinforcing ratios				*Base Connect*
								BE		Web		
		Uni-directional[A]	*Bi-directional*[B]	*Axial Load Ratio*[C]	ℓ_w/t_w	ℓ_f/t_f	ℓ_f/t_w	$\rho_{BE,\ell}$	$\rho_{BE,con}$	$\rho_{web,\ell}$	$\rho_{web,h}$	
Sittipunt & Wood [10]	CLS	WA		5.9	20.00	12.00	0.60	4.45	0.84	0.29	0.27	Cold joint
	CMS	WA		6.5	20.00	12.00	0.60	4.45	0.84	0.55	0.54	Cold joint
Ile & Reynouard [11]	IleX	SA		10.3	6.00	5.00	0.83	1.01	0.80	0.15	0.43	Cold joint
	IleY	WA		10.3	6.00	5.00	0.83	1.01	0.80	0.15	0.43	Cold joint
	IleXY		CL	11.7	6.00	5.00	0.83	1.01	0.80	0.15	0.43	Cold joint
Beyer et al. [2]	TUA		SA,WA, 45,CL	2.2	8.67	7.00	0.81	1.48	1.46	0.23	0.30	Keyed
	TUB		SA,WA, 45,CL	4.4	13.00	10.50	0.81	2.17	1.91	0.36	0.45	Keyed
Lowes [12]	CW1	SA		5.0	20.00	8.00	0.40	3.57	1.24	0.26	0.73	Cold joint
	CW2		SA,WA	5.0	20.00	8.00	0.40	3.57	1.33	0.26	0.73	Cold joint
	CW3		SA,WA	5.0[D]	20.00	8.00	0.40	3.57	1.33	0.26	0.73	Cold joint

[A] SA = Strong Axis, WA = Weak Axis.
[B] 45 = loading 45 to leg, CL = cloverleaf of similar pattern.
[C] Axial load ratio is calculated as $\%A_g f_c$'.
[D] Axial load varies in weak axis loading (−6.4 to 16.0%).

wall pier. Other wall tests included bi-directional loading; however, the walls' reinforcement ratio and normalized geometry (e.g., l_w/t_w) were either much smaller than modern construction [11] or there was no reference uni-directional test [2]. These results indicate that although the prior tests are very informative, there are significant gaps in the C-shaped wall database as a whole, in particular understanding the impact of complex loading conditions in comparison to simple loading conditions and realistic geometries relative to building construction.

3. C-shaped wall test program

This study examines the seismic response of non-planar, C-shaped concrete walls common in modern mid-rise buildings on the West Coast. There were three nominally identical test specimens. Because of the timing of the test program, the walls were designed using the ACI 318-08 Code [13] and are compliant with ACI 318-19 Code, except for the horizontal spacing of confining reinforcement which slightly exceeded the 2b/3 requirement per Fig. R18.10.6.4.a of ACI 318-19 [1]. The test series investigated the effects of uni-directional (CW1) and bi-directional (CW2) loading on an isolated C-shaped wall, and bi-directional loading of a C-shaped wall in a coupled core-wall system (CW3). In that way, each subsequent wall specimen was accessed using the result of the prior test, since the prior test used simpler loading.

The full-scale wall design was based on the average dimensions found from a review of thirteen buildings with coupled-wall systems designed for construction on the West Coast from 1991 through 2007; approximately half of these systems used C-shaped walls [14,15]. The methodology used to design was developed with input from practicing engineers. The wall geometry and loading needed to meet the constraints of the NSEL laboratory and the configurations of wall tested in the prior two phases of the program. (See Lowes et al. [5] for more information on the first planar-wall phase and see Lehman et al. [6] for more information on the second, coupled-wall phase.)

Fig. 1 shows a building plan view with the prototype C-shaped wall in the coupled core-wall configuration. The wall specimens were approximately 1/3 of full scale where the full-scale wall had 3.7 m (12 ft.) story heights, a 9.1 m (30 ft.) total wall length, 3.7 m (12 ft.) long flanges, and had 460 mm (18.0 in.) thick walls. The 1/3 scale test specimens therefore had story heights of 1.2 m (4 ft.), wall length of 3.0 m (10 ft.), 1.2 m (4 ft.) long flanges, and 150 mm (6 in.) thick walls. To meet size constraints of the NSEL MUST-SIM facility and to physically simulate the regions in which inelastic action was expected to occur, the specimens were designed to represent the bottom three stories of the 10-story prototype wall. The load and boundary condition boxes (LBCBs) available at the facility enabled application of overturning moment, shear, and axial load to account for the gravity and lateral loads imposed on the upper seven stories of the prototype wall. The distribution of lateral earthquake forces was based on the ASCE 7 [16] equivalent lateral force (ELF) distribution (Fig. 2). This determined the moment-to-shear ratio for the isolated C-shaped walls and the simulated coupled core wall system. The target axial load was approximately 5% of the gross axial capacity ($0.05A_g f'_c$), equal to 1360 kN (306 kips). For the wall with simulated coupling action, the moment-to-shear ratio and target axial load were varied in the weak-axis loading direction to simulate the variation in tension or compression axial demands resulting from the wall acting as a pier in the coupled core-wall system. Based on numerical simulations, the distribution of shear, moment and axial load on the wall pier were varied at key points in the loading history including cracking, yielding and other damage limit states to simulate the varying stiffness of the coupling beams.

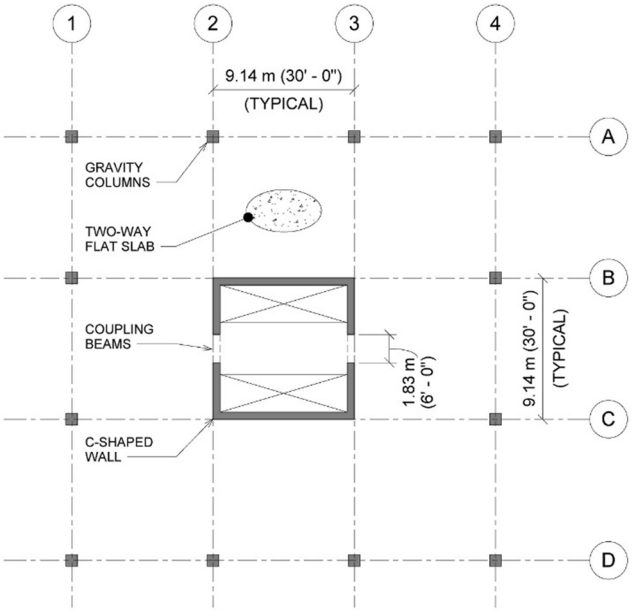

Fig. 1. Building plan with prototype C-shaped coupled core wall system.

3.1. Code-based design of wall specimens

As indicated previously, the test specimens have nominally identical designs. Fig. 3 and Table 1 provide the geometry and reinforcement details for the walls. Details of the design process are provided in Lowes et al. [12]; the following is a summary.

1. *Wall Geometry*. The length and thickness of the wall web was selected to match planar walls [5] tested in an earlier stage of research, which would allow comparison of between planar and uni-directionally loaded C-shaped walls. The flange length was selected as 40% of the wall web length.
2. *Loading*. The ASCE 7 [16] ELF distribution for the 10-story prototype wall was assumed, resulting in relationship between the base moment and shear demand of $M_u = V_u H_{eff} = 0.71 V_u H_{10}$. In this expression, H_{10} is the height of the 10-story wall and the 0.71 factor follows from the ELF distribution for a building with uniform mass and stiffness. M_u and V_u are the moment and shear demand, respectively, resulting from the lateral load distribution.
3. *Flexural Design for Strong-axis Loading Direction.* The boundary element and web longitudinal reinforcement was designed such that $\phi M_n \geq M_u$ with a flexural strength reduction factor of $\phi = 0.9$. where M_n is the nominal strength defined by ACI. The web longitudinal reinforcement of 0.26% was selected to be approximately equal to the ACI Code minimum of 0.25%. The boundary element and gross

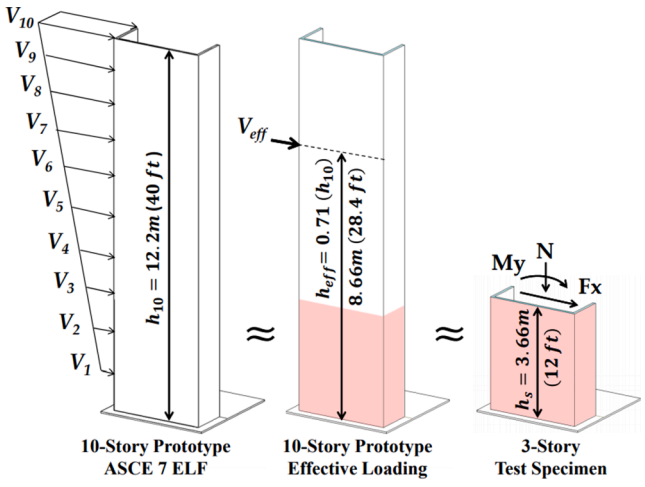

Fig. 2. Geometry and load distribution of isolated prototype wall and test specimen.

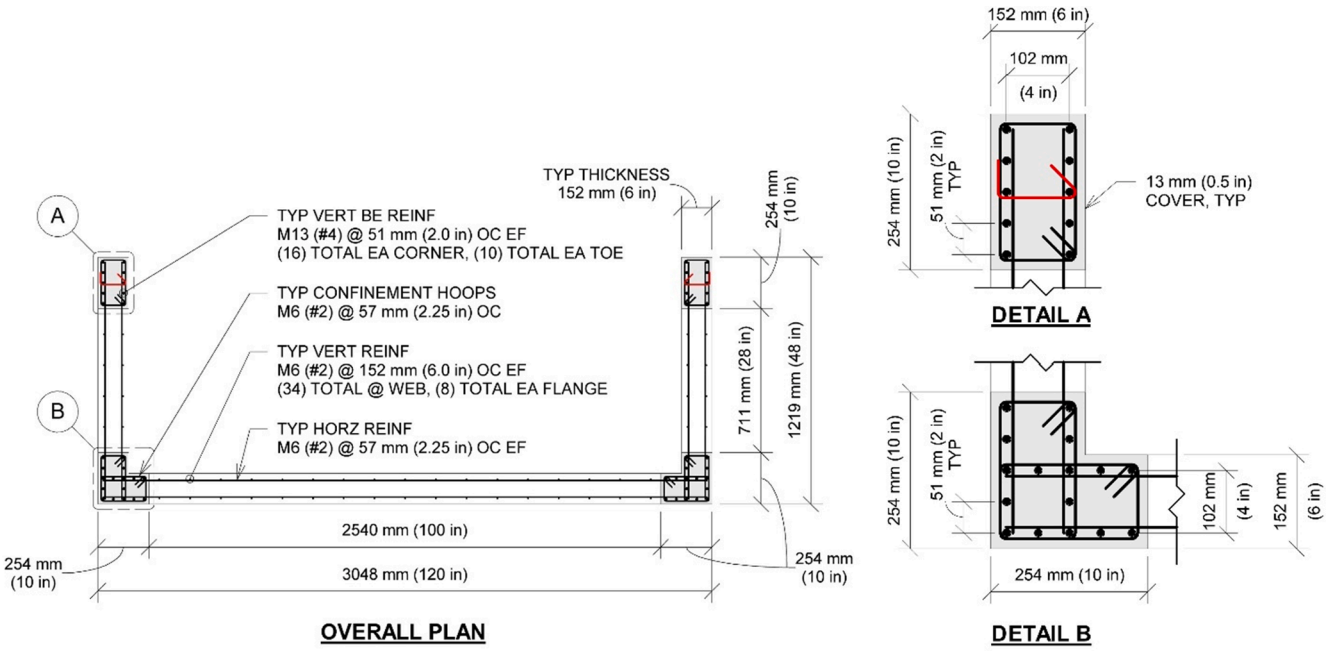

Fig. 3. Geometry and reinforcement for C-shaped walls with boundary element details.

longitudinal reinforcement ratios were selected to represent modern West Coast wall design [17].

4. *Flexural Design for Weak-axis Loading Direction.* For desirable performance of coupled walls in a core-wall system it is recommended to use a degree of coupling less than 55% [18]. A target degree of coupling of 50% was used for the specimen design.
5. *Shear Design.* A capacity-based design approach was implemented where the shear demand V_u associated with the nominal flexural strength M_n was calculated. Then the wall was designed such that $\phi V_n \geq V_u$ where $\phi = 0.75$. The resulting horizontal reinforcement ratio was approximately 0.73%.
6. *Detailing Design.* The scaled wall specimen had 25.4 cm (10 in.) long boundary elements at both web-flange intersections and flange ends. The confinement for these regions were designed according ACI 318-08 [13] for special structural walls. Note that the cross-tie shown in Fig. 3 in red on the Overall Plan and Detail A was left out during the construction of the first wall specimen, but the cross-tie was included in later specimens.

The wall specimens were designed for a nominal concrete compressive strength of 34.5 MPa (5 ksi) and reinforcing steel of 414 MPa (60 ksi). Table 2 summarizes the concrete properties for each of the wall specimens. The concrete compressive strength, f_c', and ultimate strain values, ε_{cu}, were the average of measurements from three cylinders. The values of the tensile strength, $f_r$were determined from multiple modulus of rupture beam tests. Values for concrete elastic (E_c) and shear (G_c) moduli were derived from the cylinder or beam tests. Table 3 provides the reinforcement stress–strain characteristics for each bar size, including: yield stress (f_y) and strain (ε_y), strain at the onset of hardening (ε_{sh}), as well as ultimate stress (f_u) and strain (ε_u). The steel stress–strain curves for CW1, CW2, and CW3 are available in Lowes [12]. Tables 2 and 3 also include PW4, a planar wall tested by Lowes et al. [5], which will later be used as a point of comparison to the C-shaped wall tests.

Table 2
Measured concrete material properties.

Specimen	f'c (Mpa)	εcu	fr (Mpa)	Ec (Mpa)	Gc (Mpa)
PW4	29.5	0.0021	3.4	25.73	10.72
CW1	34.3	0.0024	4.8	27.66	11.53
CW2	36.3	0.0022	4.9	28.53	11.89
CW3	35.3	0.0028	7.0	28.16	11.73

Table 3
Measured steel reinforcement properties.

Specimen	Bar size	fy (Mpa)	εy	εsh	fu (MPa)	εu
PW4	#2	522.7	0.0026	0.015	653.3	0.058
	#4	463.4	0.0023	0.0075	756.1	0.13
All CW	#2	531.7	0.0027	0.023	593.2	0.12
Specimens	#4	441.9	0.0022	0.017	630.5	0.17

3.2. Test setup & loading protocol

A pair of Load and Boundary Condition Boxes (LBCBs) were utilized to apply displacements and forces at a control point located at the geometric centroid of the wall specimens at the top of the third story. The six degree-of-freedom control capabilities of the LBCBs provide the ability to apply complex bi-directional loading of any combination of displacements and forces. Fig. 4 shows the configuration of the test setup and the C-shaped wall specimen in place.

The primary study variable for the test program was displacement history. Fig. 5 serves as a reference for subsequent discussion of displacement loading patterns. For the isolated wall specimens: Specimen CW1 was subjected to uni-directional lateral loading in the strong-axis direction (typical cycle: O → A → B → O along × axis only) and a constant axial load of $0.05A_g f'_c$. The load history for Specimen CW2 built on this test and was subjected to a cruciform bi-directional lateral loading along both principal axes of the specimen (typical cycle: O → A → B → O → C → D → O) and constant axial load of $0.05A_g f'_c$. The wall specimen with simulated coupling action, Specimen CW3, was subjected to a cruciform bi-directional lateral load history. Again, this history built upon the typical cycle that was used to test Specimen CW2, and this specimen was subjected to variation in the lateral load in both directions and axial load. The loading pattern was determined prior to testing using a computational nonlinear model of a fully coupled core-wall system. Using those results, the load combination for the next cycle was computed after the completion of the prior cycle; more information can

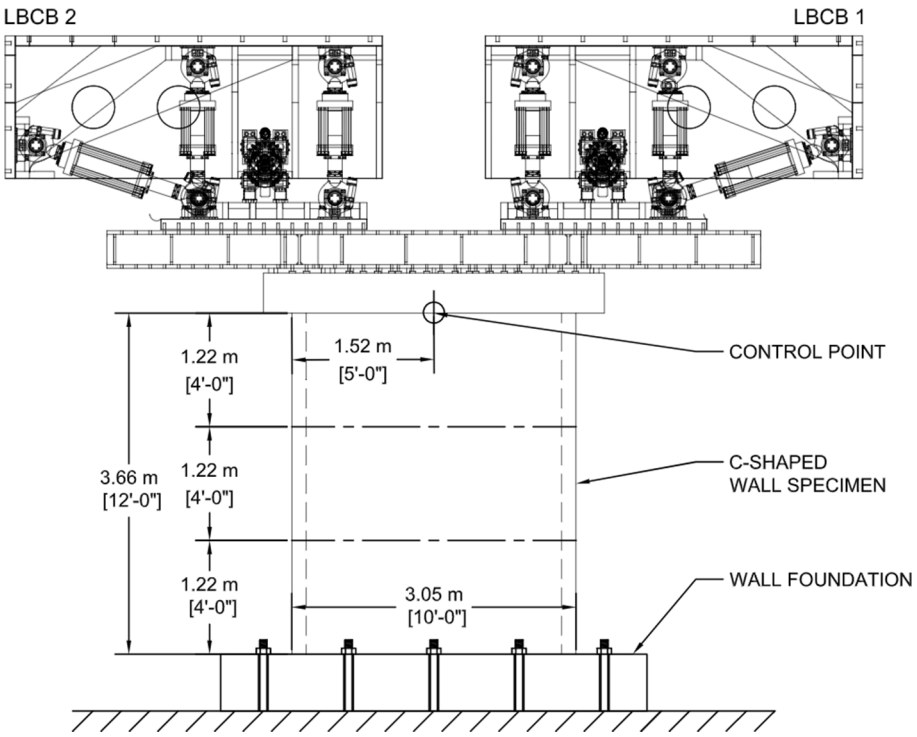

Fig. 4. Experimental setup of C-shaped wall specimen.

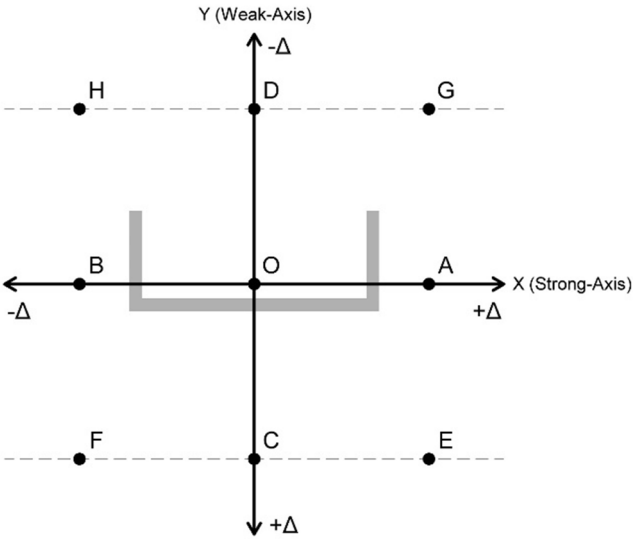

Fig. 5. Loading pattern description.

be found in Mock [20].

The lateral loading for each specimen consisted of a quasi-static, reverse cyclic displacement history. For loading in the strong-axis direction these consisted of symmetric displacement cycles and asymmetric cycles in the weak-axis direction. The maximum third-story lateral displacement for the cycles was intended to target limit states of concrete cracking, yielding of longitudinal reinforcement, nominal flexural strength, and subsequent damage states. For Specimen CW1, there was one cycle for low drift levels and two cycles for the remainder of the test beyond the cracking drift. For Specimen CW2 with cyclic cruciform loading, a majority of the test consisted of two cycles at each maximum displacement demand; however, beyond the nominal drift only one cycle was executed for each demand level. Also, towards the end of this test the displacement capacity of the LBCBs were reached in the positive and negative loading directions; therefore, the displacement pattern was modified to a bi-directional loading where a constant Y-displacement value was maintained while cycling in the X-direction (modified cycle: O → A → B → O → C → E → F → C → D → G → H → D → O).

The loading protocol for CW3 was intended to simulate a pier in a coupled core wall system. As a result the strong-axis loading is consistent with the previous wall tests (cycle: O → A → B → O). Loading the wall in the weak-axis was more complex because both the moment/shear ratio and the axial load changed. Therefore, loading required the determination of: (1) the ratio of shear, axial and moment to be applied and (2) the maximum displacement demands (for positive and negative Y-directions for each cycle). To establish appropriate demand ratios of shear, axial, and moment, numerical analyses of the 10-story prototype core-wall system subjected to increasing lateral load and constant gravity load were conducted. The demand ratio versus roof drift histories developed from these analyses were simplified for use in testing. Originally, it was believed that the displacement demands in the positive and negative Y directions could be of equal magnitude, but as testing progressed the specimen stiffness under positive Y direction loading varied substantially from that of the negative Y direction loading. Therefore, the applied loading under each of these cases did not, when combined, represent an equilibrium state for the total core-wall system (Fig. 6 illustrates free-body diagrams for the full system and individual wall piers). For this reason, the test logic was modified such that the specimen was loaded in the negative Y direction to reach an equilibrium state with the previously recorded axial load and moments at the target drift demand in the positive Y direction. Consequently, the forces imposed in each direction were in equilibrium for a cycle of loading, but the imposed displacements were of different magnitudes.

Fig. 7 summarizes the strong- and weak-axis displacement history for all three walls, and the variable axial load for CW3 (recall that CW1 and CW2 have a constant axial load of $0.05A_g f_c'$). Additional details on the loading protocols, including detailed target drift tables, are provided in Lowes et al. [12].

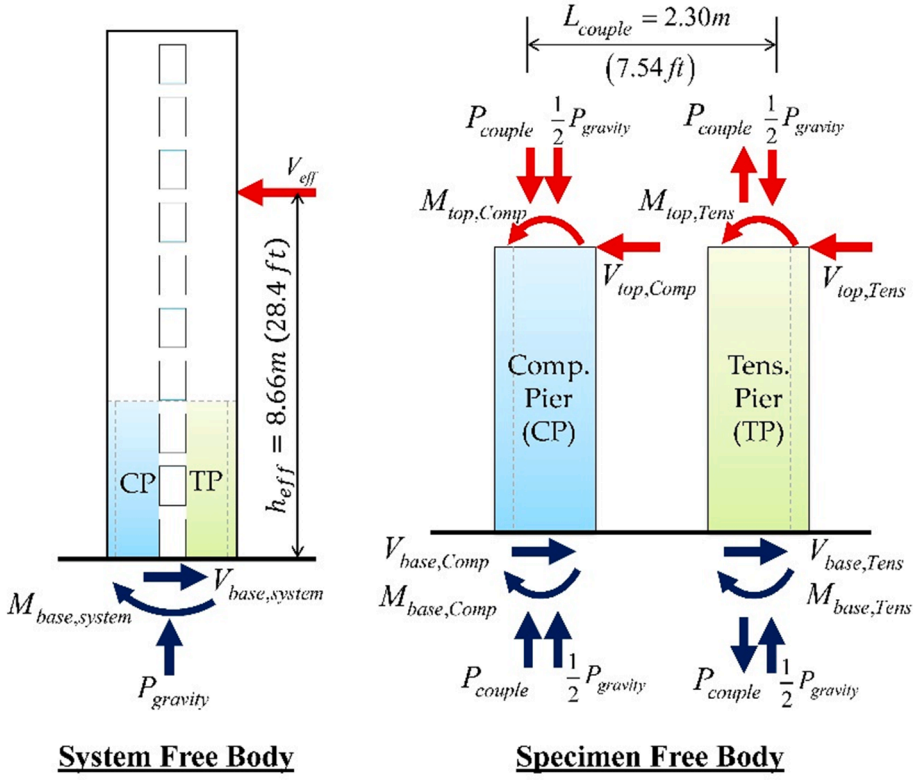

Fig. 6. Free body diagram for 10-story coupled wall system and 3-story wall pier specimen (subject to compression or tension).

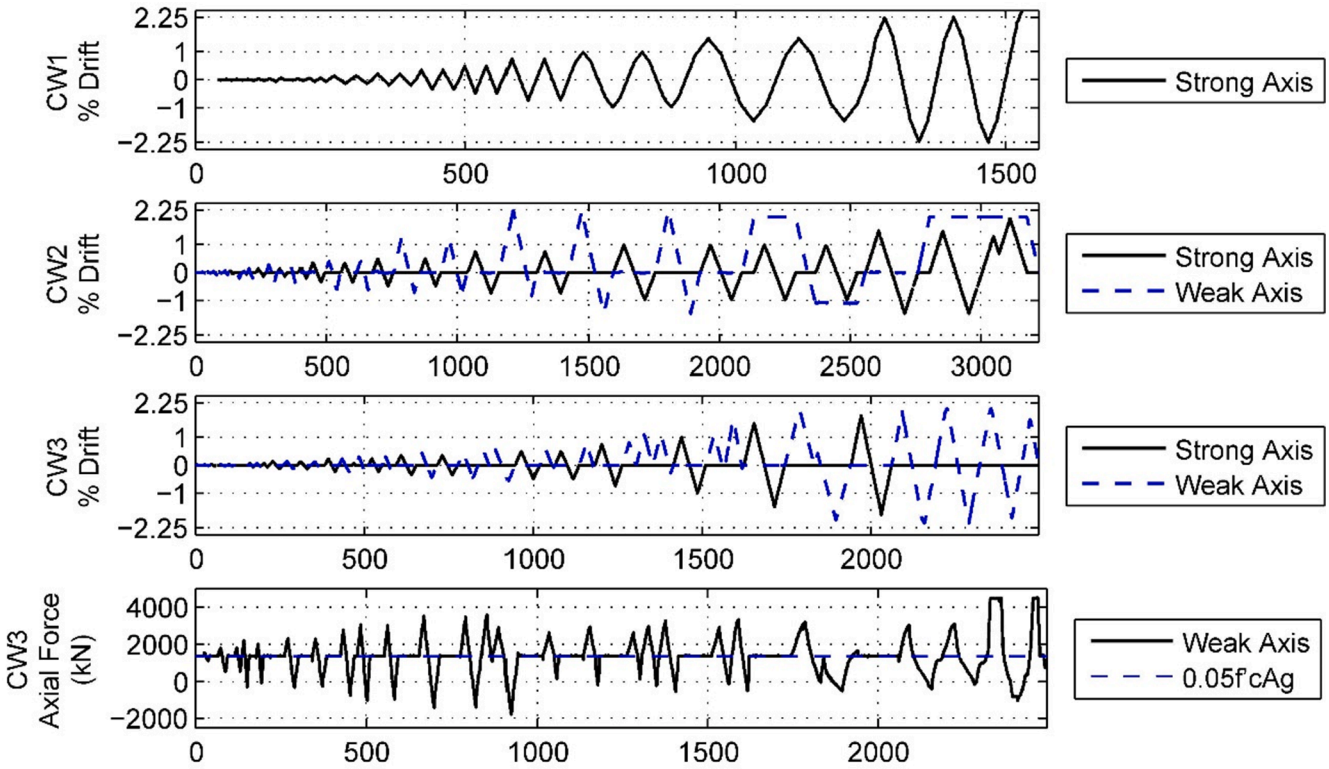

Fig. 7. Loading protocols for C-shaped wall specimens (Notes: X-axis for plots is the load step number; axial force for CW1 and CW2 is shown as a dashed horizontal line at $0.05A_g f_c'$ on CW3 Axial Force plot).

3.3. Instrumentation

The test specimens were monitored with a dense, high-resolution sensor array to capture a level of local and global wall deformation that enables validation and calibration of nonlinear finite element models. The traditional instrumentation utilized in the tests were: (1) concrete surface strain gauges, (2) strain gauges affixed to longitudinal, horizontal, and confining steel reinforcement, (3) linear potentiometers mounted to the wall in vertical and diagonal orientations to measure relative displacement, (4) string potentiometers to monitor absolute in- and out-of-plane displacement of the specimens, and (5) high-resolution linear potentiometers to calculate the six degree-of-freedom motion about the control point (Fig. 4).

Additionally, full-field non-contact measurement systems were utilized. For all tests, two Nikon Metrology/Krypton coordinate measurement cameras were used to capture the location of light-emitting diode (LED) targets glued to the wall surface on the bottom two stories of the web and east flange [approximate grid spaced 279.4 mm (11 in.) vertically and 203.2 mm (8 in.) horizontally]. An additional photogrammetric system was utilized for Specimens CW2 and CW3. Ten high-resolution Nikon D80/D90 cameras with overlapping fields of view were used to track the position of targets affixed to the wall surface at all three stories of the web and west flange [targets are 69.85 mm by 76.2 mm (2.75 in. by 3 in.) and spaced on a grid 279.4 mm (11 in.) vertically and 228.6 mm (9 in.) horizontally]. Images captured by the photogrammetric system also document progression of cracking and spalling throughout tests. Details on the instrumentation can be found in Lowes et al. [12], Behrouzi [19], and Mock [20].

4. Observed and measured global response

The C-shaped wall tests provided experimental data that characterize the seismic response of modern, singly-symmetric non-planar walls subjected to uni- and bi-directional displacement histories. The data presented in the following sections include a summary of the global load-deformation response and damage progression of each specimen. For a detailed discussion of the C-shaped wall response, the reader is referred to following documents: Lowes et al. [12], Behrouzi [19], and Mock [20]. Comprehensive laboratory datasets as well as support documentation for each test is available on the NHERI Project Warehouse [7–9].

Fig. 8 shows the normalized base moment (ratio of measured base moment to calculated nominal moment, M_b/M_n) versus drift at the top of the 10-story wall for each of the specimens. For bi-directionally loaded CW2 and CW3, these plots include response in both the strong and weak axis directions. Drift at the tenth story is the displacement normalized by the 10-story height. Displacement at the tenth story is calculated as the lateral displacement measured at the top of the third story and elastic deformation of the upper seven stories using a Timoshenko beam model with an effective stiffness of $0.35E_cI_g$ for the flexural stiffness and $0.15G_cA_{cv}$ for the shear stiffness. The nominal moment strength, M_n, of each specimen was calculated per ACI 318-19 [1] using the measured material properties in each of the principal directions of loading and is indicated in Table 4. These calculations use the assumption that strain distribution is linear along the length of the wall (or, flanges in the case of weak-axis loading). Note that positive/negative drift and designations of strong/weak-axis loading correspond to the notation defined previously in Fig. 5 describing the loading patterns.

For the normalized base moment-drift plots provided for Specimen

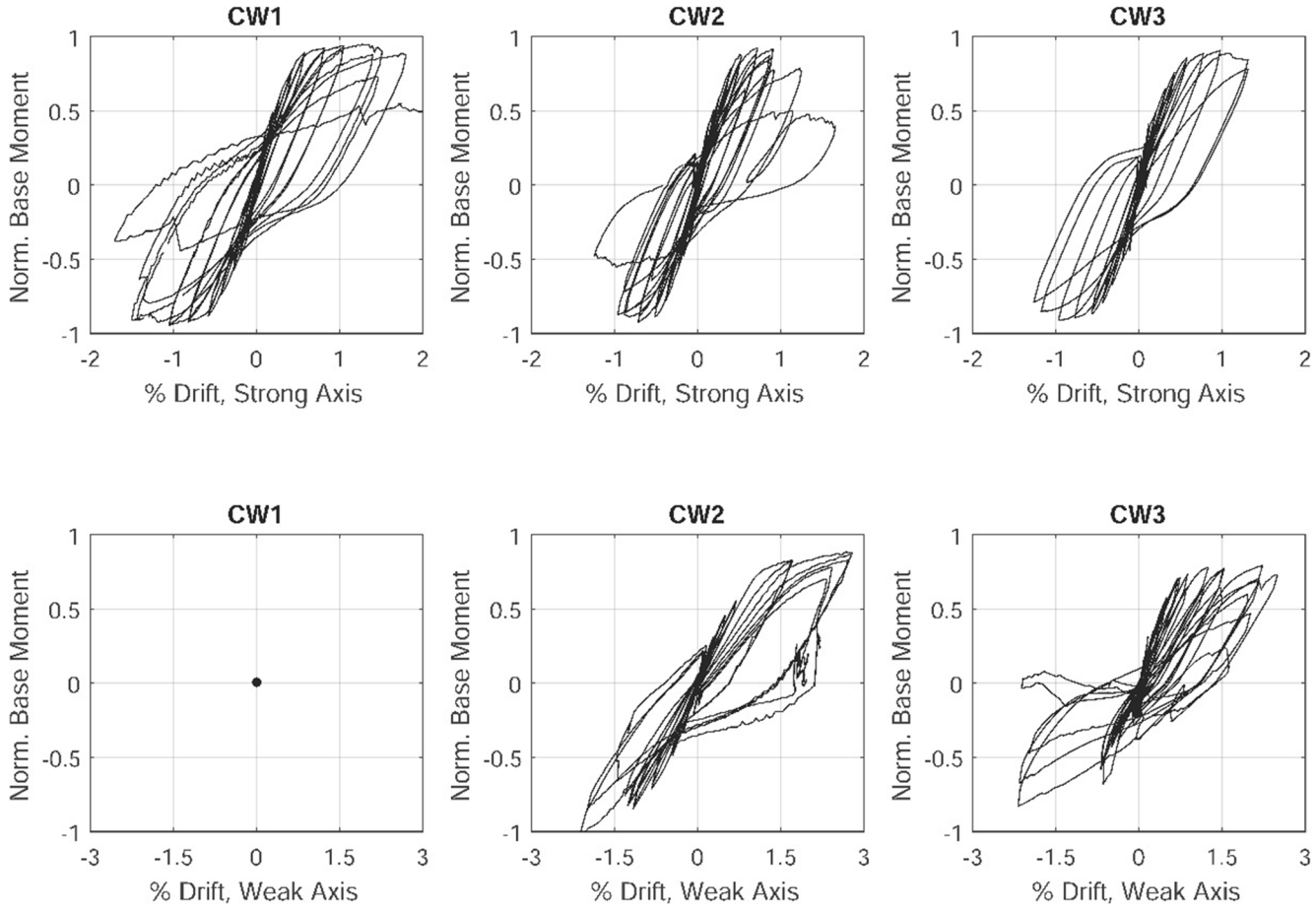

Fig. 8. Normalized base moment versus 10-story drift in strong and weak-axis directions.

Table 4
C-shaped wall demands and capacities.

(a) Strong axis

Specimen ID	ACI shear strength, V_n^A	Max shear demand, V_{max}^A	V_{max}/V_n	Design strength, M_n, k -ft (kN m)	Max moment, M_{max}, k -ft (kN m)	M_{max}/M_n
CW1	$5.8\sqrt{f'_c}A_g(0.48\sqrt{f'_c}A_g)$	$2.5\sqrt{f'_c}A_g(0.21\sqrt{f'_c}A_g)$	0.44	6414 (8696)	6080 (8243)	0.95
CW2	$5.6\sqrt{f'_c}A_g(0.47\sqrt{f'_c}A_g)$	$2.4\sqrt{f'_c}A_g(0.20\sqrt{f'_c}A_g)$	0.42	6426 (8712)	5949 (8066)	0.93
CW3	$5.7\sqrt{f'_c}A_g(0.47\sqrt{f'_c}A_g)$	$2.4\sqrt{f'_c}A_g(0.20\sqrt{f'_c}A_g)$	0.41	6421 (8706)	5851 (7933)	0.91

[A] Units: f'_c in psi (f'_c in MPa)

(b) Weak axis (+Y, end of flange in tension)

Specimen ID	ACI shear strength, V_n^A	Max shear demand, V_{max}^A	V_{max}/V_n	Design strength, M_n, k -ft (kN m)	Max moment, M_{max}, k -ft (kN m)	M_{max}/M_n
CW2	$4.9\sqrt{f'_c}A_g(0.41\sqrt{f'_c}A_g)$	$0.6\sqrt{f'_c}A_g(0.05\sqrt{f'_c}A_g)$	0.13	1733 (2350)	1525 (2068)	0.88
CW3	$5.0\sqrt{f'_c}A_g(0.42\sqrt{f'_c}A_g)$	$1.9\sqrt{f'_c}A_g(0.16\sqrt{f'_c}A_g)$	0.38	2048 (2777)[B]	1613 (2187) [B]	0.79[B]

[A] Units: f'_c in psi (f'_c in MPa)[B] Axial load = 746 kip (3318 kN) compression

(c) Weak axis (−Y, end of flange in compression)

Specimen ID	ACI shear strength, V_n^A	Max shear demand, V_{max}^A	V_{max}/V_n	Design strength, M_n, k -ft (kN m)	Max moment, M_{max}, k -ft (kN m)	M_{max}/M_n
CW2	$4.9\sqrt{f'_c}A_g(0.41\sqrt{f'_c}A_g)$	$1.0\sqrt{f'_c}A_g(0.09\sqrt{f'_c}A_g)$	0.21	2538 (3441)	2549 (3456)	1.0
CW3	$5.0\sqrt{f'_c}A_g(0.42\sqrt{f'_c}A_g)$	$1.3\sqrt{f'_c}A_g(0.11\sqrt{f'_c}A_g)$	0.27	1717 (2328) [B]	1434 (1944) [B]	0.84[B]

[A] Units: f'_c in psi (f'_c in MPa)[B] Axial load = 114 kip (507 kN) tension

CW3 in Fig. 8, it is important to recognize that the nominal moment, M_n, for the weak-axis direction loading varies throughout the imposed displacement history. This is due to the simulated coupling-action where the physical specimen is treated as the tension or compression pier and is subject to a variable axial load. Therefore, a sectional analysis was conducted to develop the full moment-axial load interaction curve for the wall specimen. From this curve, an expression for linear fit was developed for the range of axial load applied to the compression pier, $M_n = 0.232F_z + 448.7$ (kN-m), and a separate expression was similarly determined for the tension pier, $M_n = -0.581F_z - 592.8$ (kN-m). In each function, F_z is the applied axial load at a particular load step during the test.

Table 4 lists the maximum shear and moment carried by the walls and the nominal capacities calculated via ACI 318-19 [1]. These values are reported separately for strong-axis, weak-axis negative, and weak-axis positive loading directions.

4.1. CW1: Uni-directional loading

The first C-shaped wall specimen was tested as an isolated wall assembly and was subjected to a uni-directional displacement history in the strong-axis direction with constant axial load. The objective of this test was to: (1) contribute a detailed dataset measuring the response the uni-directional behavior of C-shaped geometries simulating geometries found in modern RC wall building construction, and (2) generate a baseline of comparison for both a previously tested the planar wall Specimen PW4 and the subsequent bi-directional C-shaped walls CW2 and CW3 in this test program. (Note X drift indicates drift in the X, or web, direction.) The damage progression was as follows:

- Flexural cracking initiated in the bottom two stories of the wall flanges at 0.02% X drift, followed by diagonal shear cracking in the web at 0.10% X drift. Additional flexural cracking was observed in the web boundary element at a uniform spacing coinciding with confining hoop locations.
- Strain gauges on longitudinal reinforcement indicated the yielding of multiple No. 4 bars in the boundary elements and No. 2 bars in the flanges during the 0.35% X drift cycle.
- During the 0.75% X drift cycle, vertical cracking developed along the interior edge of flange boundary elements and separation at the wall-foundation interface became apparent.
- During the 1.49% X drift cycle, numerous No. 2 bars in the web and flanges fractured, significant cover spalling occurred in the corner boundary elements, and No. 4 bars in the East flange boundary element buckled.
- During the second cycle at 2.25% X drift, while approaching the negative peak displacement, a large number of No. 4 bars in the East flange boundary element fractured leading to a drop in wall strength. Significant web sliding and some core crushing in corner boundary elements were observed.
- A final monotonic push was conducted. The final failure occurred at +3.52% X as a result of severe buckling of No. 4 bars in the East flange boundary element and successive rupturing of No. 4 bars in West flange boundary element.

Fig. 8 shows the measured response of the specimen; the wall was able to reach a maximum base moment of $0.95M_n$ and the maximum average shear stress demand was $0.21\sqrt{f'_c}A_g$ MPa ($2.5\sqrt{f'_c}A_g$ psi). Loss of lateral strength was due to buckling-fracture of longitudinal reinforcement in corner boundary elements. There was notable crushing of the flanges after sliding occurred and No. 2 bar fracture in the web. Fig. 9 (a) shows the wall at the end of the test. A video of the test of Specimen CW1 is available on YouTube: https://youtu.be/ZJZ1veGWmVo.

4.2. CW2: Bi-directional loading

The second C-shaped wall specimen was also tested as an isolated wall; it was subjected to a bi-directional cruciform displacement history with constant axial load. The objective of this test was to generate a robust data-set to characterize the seismic behavior of a bi-directionally loaded, singly-symmetric non-planar wall geometry and to provide a direct comparison to Specimen CW1. The damage progression is as follows:

- Flexural cracking initiated in the bottom two stories of the wall flanges at 0.03% X drift, followed by diagonal shear cracking in the web at 0.07% X drift. Damage in the Y-direction loading consisted of reopening of these cracks, new horizontal and diagonal cracks due to weak-axis loading at +0.06% and +0.14% Y drift, respectively.
- Strain gauges on longitudinal reinforcement indicated the yielding of multiple No. 4 bars in the bottom two floors of boundary elements in each direction and No. 2 bars in the web and flanges during the 0.35% X drift (+0.42% and −0.63% Y) cycles. Separation at the wall-foundation interface was visible.
- During the 0.75% X (+2.25% and −1.49% Y) drift cycle, some of the No. 2 bars in the web of the wall buckled, in particular the bars in the far curtain of longitudinal reinforcement in the web. Spalling was observed in the web and the ends (sometimes referred to as toes) of the flanges approximately two feet above the footing.

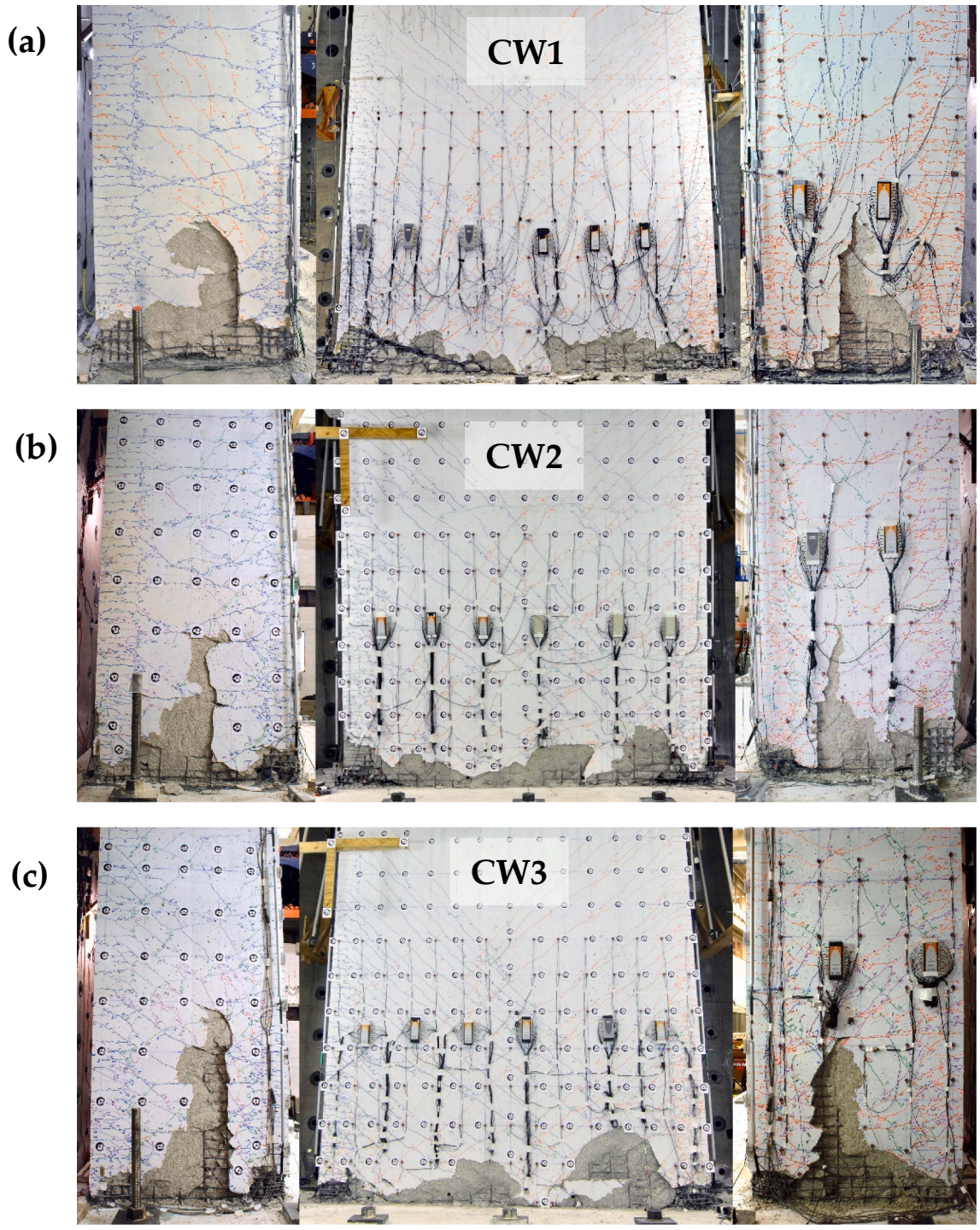

Fig. 9. Specimens after completion of testing. Ultimate drift at top of specimen (3rd-story drift). (a) CW1: +3.52% 3rd Story Drift, (b) CW2: +1.9% X and +2% Y-direction 3rd story drift, (c) CW3: +1.63% X and −2.75% Y-direction 3rd story drift.

- During the 1% X (+2% and −1.1 Y) drift cycles, numerous No. 2 bars in the web had ruptured, and No. 4 bars in the boundary element had begun buckling.
- During the X-direction pushover to 1.9% X drift (while maintaining +2% Y drift), approximately five No. 4 bars in the West flange boundary elements fractured. Loss of core confinement was extensive in corner boundary elements and buckling of longitudinal rebar in the East boundary elements was significant. There was one instance of hoop fracture in the Northeast corner boundary element.

Fig. 8 shows the measured response of the specimen; the wall was able to reach a maximum base moment of $0.93M_n$ in the strong-axis direction, $0.88M_n$ for the positive weak-axis direction, and $1.0M_n$ for the negative weak-axis direction. The maximum average shear stress demand in the strong-axis direction was $0.20\sqrt{f_c'}A_g$ MPa ($2.4\sqrt{f_c'}A_g$ psi), with stress demands in the positive weak-axis direction of $0.05\sqrt{f_c'}A_g$ MPa ($0.6\sqrt{f_c'}A_g$ psi) and negative weak-axis direction of $0.09\sqrt{f_c'}A_g$ MPa ($1.0\sqrt{f_c'}A_g$ psi). Again, loss of lateral strength was attributable to buckling-rupture of longitudinal reinforcement in corner boundary elements. As with CW1, there was significant sliding along the

large separation that formed at the wall-footing interface. There was subsequently considerable crushing of the flanges and No. 2 bar fracture in the wall web. Fig. 9(b) shows the wall at the end of the test. A video of the test of Specimen CW2 is available on YouTube: https://youtu.be/M-CWPVWB8Pw.

4.3. CW3: Bi-directional loading with simulated coupling

The final C-shaped wall specimen was tested as part of a simulated coupled core-wall system; it was subjected to a bi-directional cruciform displacement history with variable axial load. The objective of this test was to simultaneously examine bi-directional loading and the effects of coupling two C-shaped walls (as is common in building cores). There have been prior tests examining coupling action in concrete walls, these have primarily consisted of planar wall piers (and infrequently walls with enlarged boundary elements [21,22]). The focus of these prior studies has been on the performance of varying coupling beam configurations and the influence of coupling on the response of the wall piers. The damage progression of CW3 was as follows:

- Flexural cracking initiated at 0.02% X drift, followed by diagonal cracking at 0.07% X drift. Y-direction loading consisted of reopening of these cracks, new horizontal and diagonal cracks due to weak-axis loading was first noted at +0.05% and +0.22% Y drift, respectively.
- Strain gauges on longitudinal reinforcement indicated yielding first in No. 2 bars in the web and subsequently in multiple No. 4 bars in boundary elements during the 0.35% X drift cycle. Yielding in the boundary element was noted in the Y-direction during the 45% drift cycle.
- During the 0.75% X drift (+1.11% and −0.28% Y) cycle, minor spalling was observed on the Southeast corner boundary element in a region where the cover had been patched.
- More significant vertical splitting cracks and spalling in corners and flanges were seen in the 1.5% X drift (+1.9% and −1.9% Y) cycles. Additionally, bar buckling and rupture was observed in numerous No. 2 bars in the web and West flange. Out-of-plane shear demand on the flanges was significant enough to cause large regions of spalling near the footing.
- During the 1.78% X drift (+1.9% and −1.9% Y) cycle, crushing and loss of confinement occurred in the corner boundary elements. The first negative Y cycle resulted in one No. 4 bar rupture, and the second cycle in approximately 10 No. 4 bar fractures.
- Additional cycles in the Y-direction (+1.62% and −1.9%) resulted in further loss of confinement and core crushing in corner boundary elements. Multiple No. 4 bars fractured in the East flange at −1.53% drift and the specimen could no longer carry the full axial tension. The final positive Y direction cycle ended in a minor compressive failure.

Fig. 8 shows the measured response of the specimen; the wall was able to reach a maximum base moment of $0.91M_n$ in the strong-axis direction, 0.79 M_n for the positive weak-axis direction at a compressive axial load of 3320 kN (746 kips) and $0.84M_n$ for the negative weak-axis direction at a tensile axial load of 507 kN (114 kips). The maximum average shear stress demand in the strong-axis direction was $0.20\sqrt{f_c'}A_g$ MPa ($2.4\sqrt{f_c'}A_g$ psi)), with stress demands in the positive weak-axis direction of $0.16\sqrt{f_c'}A_g$ MPa ($1.9\sqrt{f_c'}A_g$ psi) and negative weak-axis direction of $0.11\sqrt{f_c'}A_g$ MPa ($1.3\sqrt{f_c'}A_g$ psi). Again, the wall failure resulted from rupture of longitudinal No.4 reinforcement in the tension pier and a minor compressive failure in the compression pier with a reduction in axial and shear carrying capacity. Sliding followed by flange crushing and No. 2 bar fracture in the wall web occurred in CW3 as well. Fig. 9(c) shows the wall at the end of the test.

It is important to examine the extent of damage observed in the walls after similar combined strong- and weak-axis drift demands to evaluate the effects of bi-directional loading. Fig. 10 shows Specimens CW1 and CW2 following the 1.5% X-drift and Specimen CW3 after the 1.62% X-drift (to examine similar weak-axis demands as CW2). While Specimen CW1 has more damage to wall web along the diagonal crack plane from the edge of the east boundary element to the wall-foundation interface, the damage to the flanges is notably higher in Specimen CW2 and CW3, as expected. This suggests that the increased compression and tension demand along the web due to bi-directional loading degrades the shear resisting mechanisms at the wall-foundation interface. The result is higher shear compression demand in the corner boundary elements and flanges during strong-axis loading. Damage to corner (web-flange intersection) boundary elements appears consistent for all walls when viewed from the web; however, these boundary elements show considerably more spalling from the flange sides for Specimens CW2 and CW3. Additionally, Specimen CW2 shows the most damage to the flange-end boundary element (specifically on the west flange).

4.4. Synthesis of experimental response

The three C-shaped wall specimens had similar progression of damage. In addition, all specimens had nearly identical strong-axis load-deformation envelopes up to the peak flexural strength (that is, bi-directional loading did not influence the flexural strength). However, bi-directional loading resulted in substantial differences in the drift demands at the onset of the damage limit states as well as a significant reduction in stiffness during post-yield displacement cycles.

4.4.1. Comparison of onset and progression of structural damage

The general damage mechanisms of the three walls specimens is as follows. First significant damage (following yielding of the longitudinal steel), was the onset of shear sliding at a crack at or near the wall-foundation interface (Fig. 11(a)); the crack width increases at greater demand drift levels (particularly in the strong-axis loading direction and negative weak axis loading direction). Significant local straining at this crack resulted in the fracture of a majority of longitudinal No. 2 bars in the wall and flanges. Damage to the web and the lightly-reinforced section of the flanges resulted in increased demand in the boundary elements resulting in increased deformation demand in the longitudinal bars including dowel action along the wall-foundation interface (Fig. 11(b)). The out-of-plane deformation between the flange boundary elements results in considerable spalling in the flange between the boundary elements (Fig. 11(c)). Additionally, vertical splitting cracks occur at both web and flange faces of the corner boundary elements, and separation occurs at the edge of the corner boundary elements and the wall web. This damage resulted in increased demand on the corner boundary elements resulting in local concrete crushing around the longitudinal bars and lower confining hoops in the boundary elements due to aforementioned dowel action and cycles of buckling/straightening of No. 4 longitudinal bars (Fig. 11(d) and 3). Elongation of confining hoops (with limited hoop rupture) contributed to a loss of confinement in the boundary elements (Fig. 11(e)); this damage was accompanied by crushing of core concrete and severe buckling of longitudinal No. 4 bars. Ultimately, the C-shaped walls experience significant strength loss due to fracture of previously buckled bars, and thus can be characterized as a buckling-fracture failure mechanism.

4.4.2. Damage-state comparison

In performance-based seismic design, structural damage states are quantified using with one or more engineering demand parameters, such as story drift. Here, the damage-state data for the C-shaped wall specimens are presented in Tables 5 and 6 with respect to the measured top of specimen (third story) drift.

Table 5 summarizes the onset of horizontal and diagonal cracking in the strong-axis and positive/negative weak-axis loading directions. For horizontal cracking, the ratio of base-moment demand to calculated cracking moment, M_b/M_{cr}, at the onset drift is included. Cracking

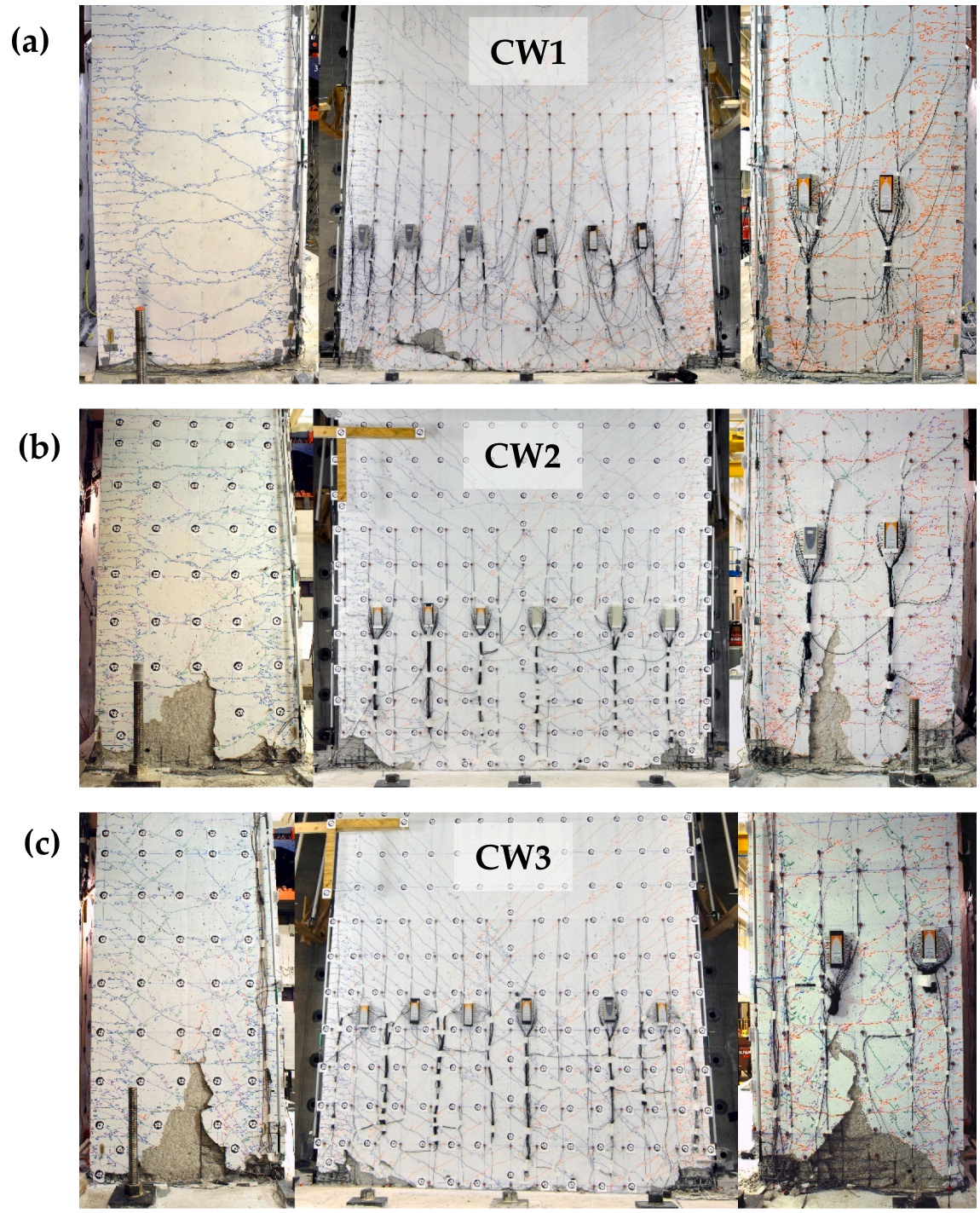

Fig. 10. Damage to specimens at similar drift demands. Drift at top of specimen (3rd-story drift). (a) CW1 (1.5% X-drift), (b) CW2 (1.5% X-drift), and (c) CW3 (1.62% X-drift).

moment is determined from an elastic sectional analysis of the C-shaped wall with constant axial load of $0.05f'_cA_g$ and moment such that the tensile stress at the extreme fiber of the concrete is equal to the modulus of rupture, approximately $0.63\sqrt{f_c'}$ MPa ($7.5\sqrt{f_c'}$ psi) [1].

For diagonal cracking, the ratio of base shear demand to $\sqrt{f_c'}A_g$ is provided, $V_b/\sqrt{f_c'}A_g$. Both horizontal and diagonal cracking initiated in the strong-axis loading direction. Limited new cracks were observed during weak-axis motion, although re-opening of strong-axis cracks was prevalent. Additional diagonal cracks were observed in Specimen CW3 during weak axis loading due to the reduced moment-to-shear ratio (resulting in a smaller effective height and higher shear demand) and reducing axial force resulting from the simulated coupling-action of a pier in a coupled wall. Specifically, horizontal cracking initiated in the strong-axis direction at drifts associated with moments between 0.3 and $0.55M_{cr}$, while diagonal cracking occurred at slightly higher drift levels. This is notably different than the onset of diagonal cracking in the weak-axis direction which occurred at significantly higher drifts than horizontal cracking in that direction.

Table 6 presents damage states beyond initial flexural/shear cracking, including: (1) initial spalling of cover concrete, (2) cover spalling that exposes reinforcement, (3) bar buckling, (4) boundary

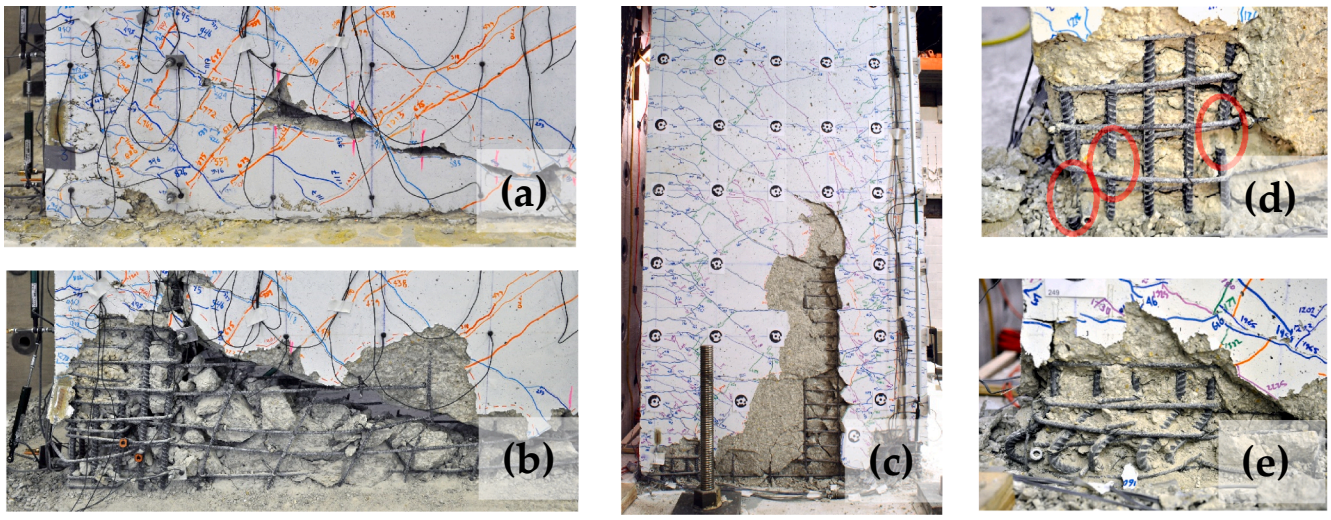

Fig. 11. Damage observed in C-shaped specimens: (a) Sliding along cracked interface and web-foundation interface, (b) dowel action in boundary elements, (c) damage to flanges, (d) Boundary element damage in web (fractured bars are circled), (e) Failure of confining reinforcement resulting from buckling of vertical longitudinal bars.

Table 5
Table of drift demands at cracking limit states. Drift at top of specimen (3rd-story drift).

State	Value	Strong axis			Weak axis (+Y, toe in tension)		Weak axis (−Y, toe in compression)	
		CW1	CW2	CW3	CW2	CW3	CW2	CW3
Horizontal Cracks	Specimen drift	0.02%	0.03%	0.02%	0.06%	0.05%	0.07%	0.07%
	M_b/M_{cr}^1	0.31	0.54	0.39	0.81	0.82	0.39	0.52
Diagonal Cracks	Specimen drift	0.10%	0.07%	0.07%	0.14%	0.22%	0.60%	0.42%
	$V_b/(A_g\sqrt{f'_c})$	1.09	1.04	1.06	0.23	1.12	0.85	0.59

Table 6
Table of drift demands at damage limit states beyond cracking. Drift at top of specimen (3rd-story drift).

Damage state	CW1	CW2	CW3
Cover spalling	1.49% X	1.44% −Y	0.75% +Y [1]
Exposed reinforcement	1.49% X	1% X and 2% +Y	1.50% +X
Bar buckling	1.49% X	2.25% +Y	1.50% +X
Core crushing	2.19% X	1.50% X	1.98% +Y
Boundary element bar fracture	2.19% X	2.50% X	1.64% −Y

[1] Spalling occurred in patched area.

element core crushing, and (5) bar fracture of longitudinal No.4 bars in the boundary elements. The third-story drifts included in Table 6 are associated with the first occurrence of each performance limit state in any of the loading directions (strong-axis: X, positive/negative weak-axis: +/−Y). The data from the three specimens indicates that drift level associated with the onset of concrete and steel damage states vary substantially and are entirely dependent on the imposed displacement history (uni-directional versus bi-directional loading).

4.4.3. Comparison of load-deformation envelope

Fig. 12 presents an envelope of normalized base moment versus top of specimen (third story) drift for all three C-shaped wall specimens in the strong-axis loading direction (Fig. 12(a)) and in the weak-axis loading direction for bi-directionally loaded CW2 and CW3 (Fig. 12 (b)). The top of specimen (third story) drift was deemed the most appropriate for comparison of relative drift capacity for Specimens CW1, CW2, and CW3 as this was the location of the displacement transducers with greatest accuracy for load control purposes. The calculation of normalized base moment and top of specimen (third story) drift are consistent with the descriptions presented in the introduction of Section 4.

All three tests had a consistent strong-axis loading protocol which allows for comparison of the influence that weak-axis loading has on strong-axis response. Fig. 12(a) shows that the strong-axis behavior is nearly identical in terms of flexural strength and stiffness up to 0.75% drift. Beyond this drift level, all walls are able to reach 91–95% of the nominal moment strength, M_n. The impact of weak-axis loading becomes apparent during the peak and post-peak inelastic response with an observed stiffness reduction in strong-axis response; the bi-directional tests also show earlier strength degradation and reduced ductility. Walls were able to maintain at least 80% of maximum strong-axis strength until: the first cycle at 2.25% X-drift for CW1; the 1.5%X-drift cycle for CW2; and the final 1.8% X-drift cycle for CW3 (substantial strength loss occurred in subsequent weak-axis cycles of CW3 leading to wall failure). The walls with constant axial load were able to maintain an axial load of $0.05A_g f'_c$ and moderate lateral load carrying capacities (40–45% of maximum strength) at relatively large drift demands (nearly 3.5% for CW1 and 2% for CW2).

The effect of weak-axis loading on strong-axis performance was most pronounced in CW2 where an initial loss in flexural capacity to about $0.68M_n$ occurred during the last 1% X-drift cycle while −1.1% Y-drift was maintained (resulting in a true bi-directional loading). The subsequent cycle at 1.5% X-drift shows an increase to $0.75M_n$ under strong-axis loading only. This was followed by another significant loss in flexural capacity to about $0.38M_n$ during the 1.5% X-drift cycle while +2.25% Y-drift was held constant (again true bi-directional loading).

Examination of the weak-axis response in Fig. 12(b) indicates that in that walls were able to reach 79–100% of the nominal moment strength, M_n. CW3 appears to have an initially stiffer response in the positive Y-direction (where the wall acts as compression pier) compared to CW2, and a softer response than CW2 when loaded in the opposite direction (tension pier). Walls were able to maintain at least 80% of maximum

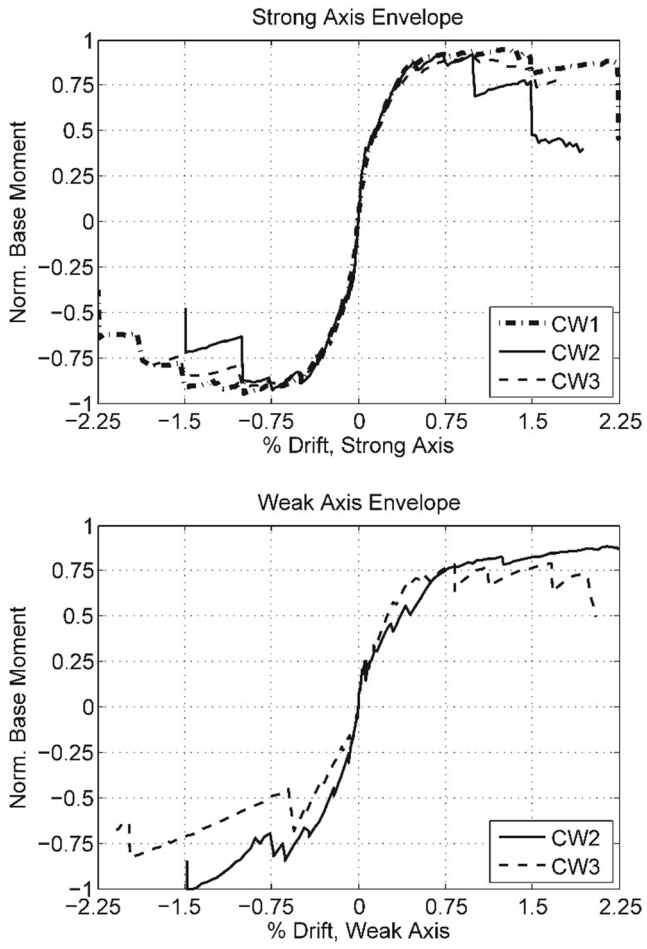

Fig. 12. Envelope of normalized base moment versus drift at Top of Specimen (third story): (a) Strong-axis for CW1, CW2, and CW3; and (b) Weak-axis for CW2 and CW3.

weak-axis strength under ***cruciform*** loading until: the final +2.25% and −1.5% Y-drift cycle for CW2; and the +2.05% and −2.09% Y-drift cycle for CW3. Of the two bi-directionally loaded walls, the wall with constant axial load (CW2) saw only a moderate strength degradation in the weak-axis direction by the final cycle with ***true bi-directional*** loading (with capacities of about 78% of the maximum strength in +Y and 70% in −Y-direction). In comparison, the wall with simulated coupled action had significant strength degradation in the weak-axis direction by the final cycle with ***cruciform*** loading (with capacities of about 30% in +Y and 18% in –Y-direction).

5. Analysis of measured response

Response of the C-shaped wall specimens was monitored using the instrumentation systems described in Section 3.3. This dense array of high-resolution sensors provides a more complete understanding of load transfer through the web/flanges, local and global damage progression as well as the final failure mechanism.

5.1. Evaluation of response using strain maps

Measured data from approximately 80 strain gauges on longitudinal reinforcement was analyzed to determine the degree of non-linear behavior in the steel for both tension and compression. The Hoehler-Stanton cyclic stress–strain model for reinforcing steel was utilized to estimate steel stresses for the experimental strain history [23]. These results were utilized to evaluate when certain thresholds were reached such as steel yield and hardening. A more detailed description of this process can be found in Birely [24].

Strain maps were created to qualitatively evaluate measured strains (relative to the aforementioned thresholds) at various steps throughout the test. The strain maps shown in Figs. 13 and 14 represent the strain state at the end of the hysteretic, or true cruciform, portion of each of the C-shaped wall tests. Fig. 13 indicates the gauges that yield in tension ($+\varepsilon_y$ and $+\varepsilon_{sh}$), and Fig. 14 shows those that yield in compression ($-\varepsilon_y$ and $-\varepsilon_{sh}$). On each map, strain gauge locations are marked with a black "x". Locations with open circles indicate initial yield strain ($\pm\varepsilon_y$), while closed circles represent strain hardening ($\pm\varepsilon_{sh}$) which suggests significant plastic deformation, finally, crosses show where yield stress ($\pm f_y$) was reached prior to/without reaching monotonic yield strain ($\pm\varepsilon_y$) due to cyclic loading. A black marker designates gauges that first reached yield strain in tension, where gray indicates compressive yield occurred first.

Tensile yielding of the longitudinal reinforcement is primarily focused in the bottom two stories for all walls with limited signs of yielding at the third floor. For CW1, plastic yielding is concentrated in or near the boundary elements for half the wall height and along the wall-foundation interface. CW2 has more widespread plastic yielding in the center of flanges for the bottom half of the wall, and less plasticity in the wall-foundation interface region (these gauges indicate steel yield, but not significant strain hardening). For CW3 available data suggests that plastic yielding was common throughout the first floor particularly in or near the boundary elements.

Compression yielding was generally limited to the bottom half of all walls, and is primarily characterized by stress yield (following tension yield) which is a result of significant cyclic response. There are fewer cases where strain yield/plasticity is observed (following tension yield); these occur mostly along the wall-foundation interface or within 41 cm (16-in) of the critical section. Compression yielding/ plasticity (before tension yield) were infrequent, and occurred along the wall-foundation interface or in the first floor. In all walls, compression (stress) yielding is concentrated in or near the boundary elements in the same locations where tensile plasticity was observed.

To compare planar and C-shaped wall response, the longitudinal strain patterns for PW4 from Lowes et al. [5] are provided in Fig. 15. The compression action in PW4 is more extensive than the C-shaped walls and is concentrated in the boundary elements at the first floor. Compressive yielding/ plasticity in the planar wall tend to initiate first, while for C-shaped walls this response follows tensile yielding/plasticity and results from repeated cycles of loading. The difference in strain patterns between these wall types suggests that the C-shaped wall flanges contribute to carrying a substantial portion of the compressive demand, thus avoiding the type of compression-controlled failures observed in the four Lowes et al. [5] planar wall specimens.

5.2. Evaluation of response based on strain fields

The high-resolution measurements collected using the Nikon Metrology/Krypton system enabled the calculation of average strain fields for the lower two floors of both the web and east flange. The LED targets were on a grid with approximately square regions, and therefore the in-plane displacement of each LED represented the deformation of the corner nodes in a four-node isoparametric quadrilateral finite element formulation. Strain fields were developed by calculating the strain at each of the nodes as described in Birely [24]. The remainder of this section summarizes observations on wall response that can be made via examination of vertical strain (ε_z) and the second principal strain (ε_1 and ε_2). In Figs. 16–18, any white regions of the strain field for the bottom two stories of the wall indicate locations where the concrete spalling led to detachment of LED sensors.

A comparison of the principal compressive strain during strong axis loading in the uni-directional test (CW1) versus the bi-directional test

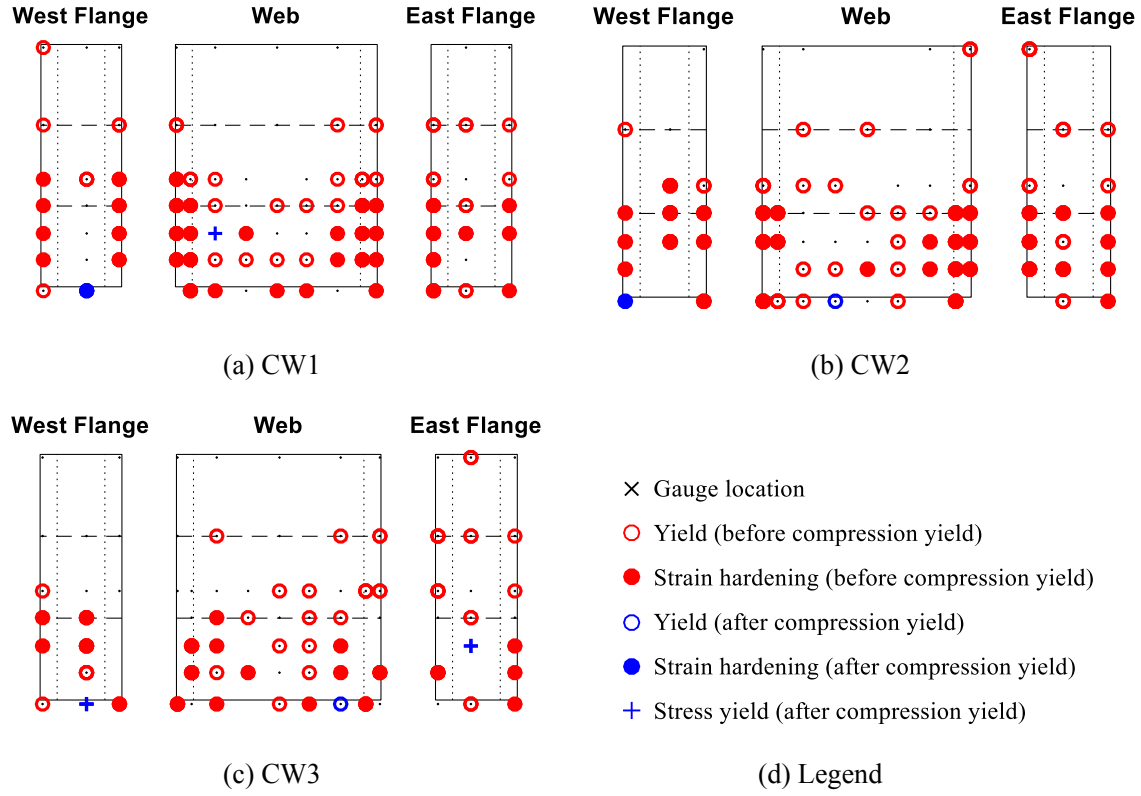

Fig. 13. Pattern of longitudinal reinforcement strain indicating ***tension*** yield. Horizontal and vertical dashed lines indicate floor levels and edges of boundary elements, respectively. (a) CW1, (b) CW2, (c) CW3, and (d) legend.

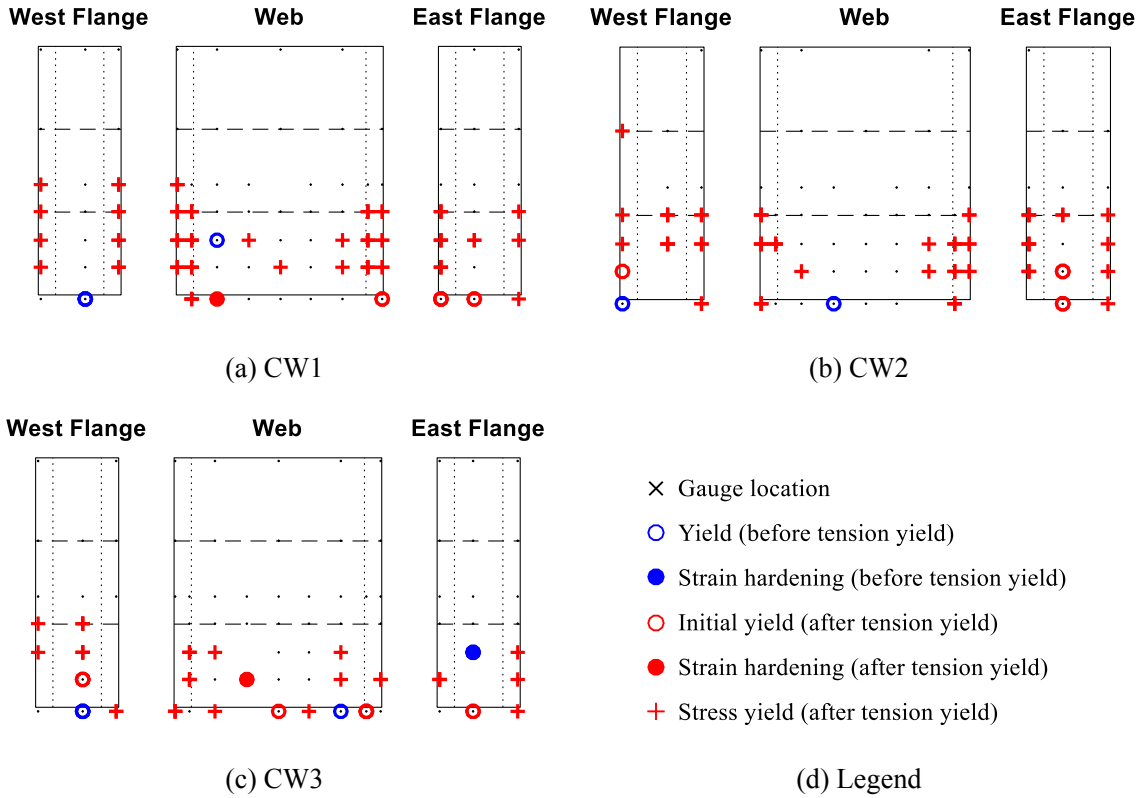

Fig. 14. Pattern of longitudinal reinforcement strain indicating ***compression*** yield. Horizontal and vertical dashed lines indicate floor levels and edges of boundary elements, respectively. (a) CW1, (b) CW2, (c) CW3, and (d) legend.

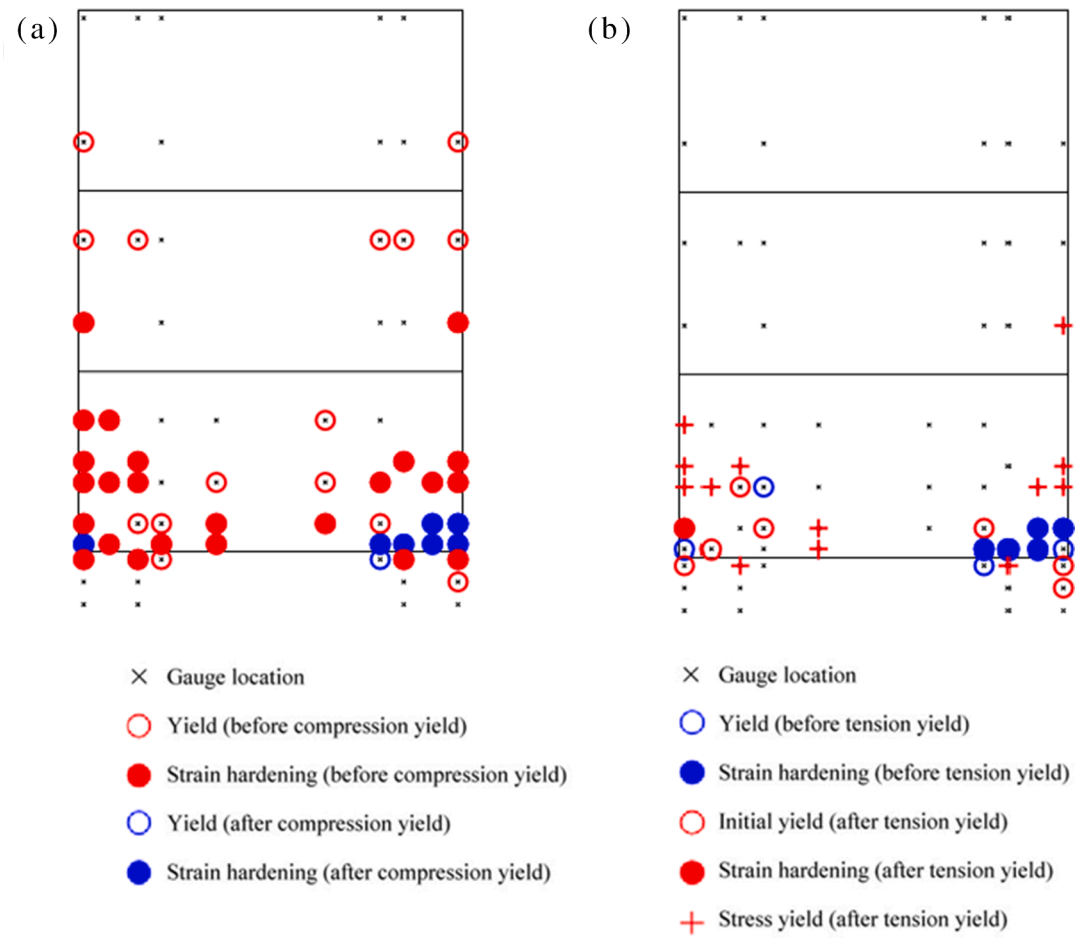

Fig. 15. Pattern of longitudinal reinforcement strain for PW4 from Lowes et al. [5]. Horizontal dashed lines indicate floor levels. (a) Indicates tension yield, and (b) compression yield.

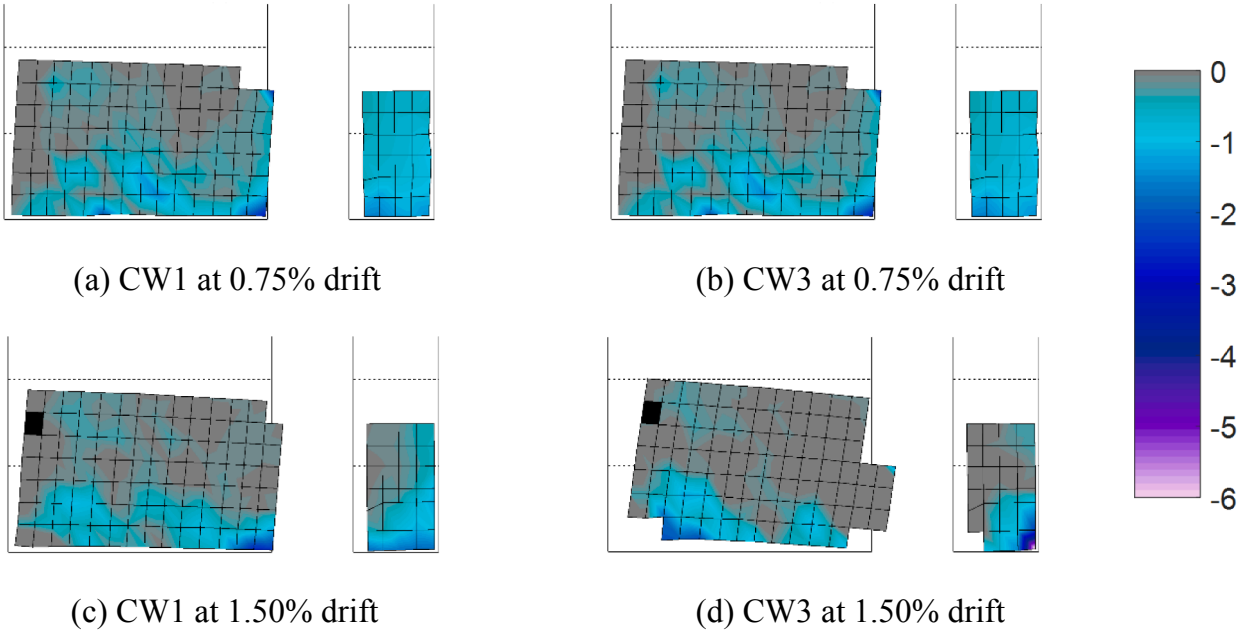

Fig. 16. Principal compressive strain in web and flange for strong axis loading (units: millistrain).

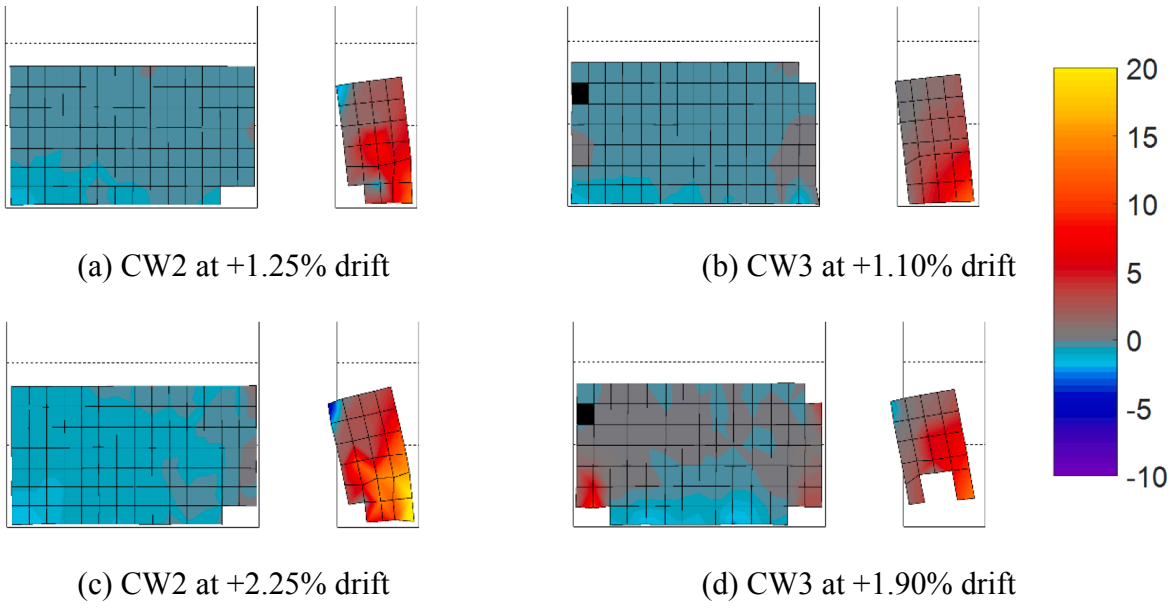

Fig. 17. Vertical strain in web and flange for weak axis loading with web compressed (units: millistrain).

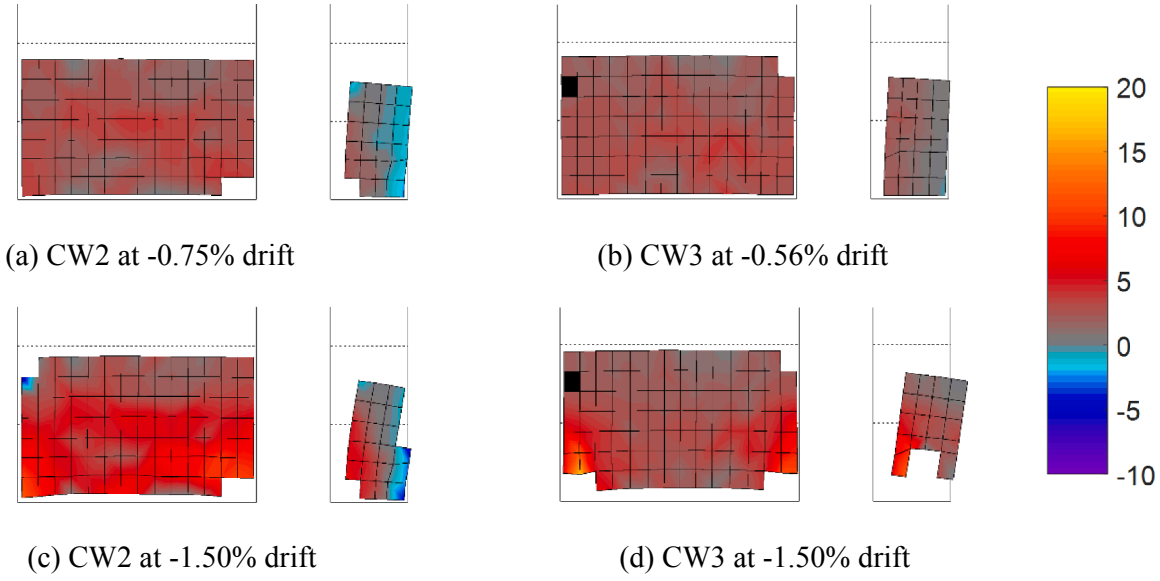

Fig. 18. Vertical strain in web and flange for weak axis loading with toe compressed (units: millistrain).

(CW3) is given in Fig. 16. The comparison at 0.75% drift reveals increased compressive stress demand in the corner boundary element of the web as well as a more non-linear strain distribution across the flange. The formation of compressive struts across the web are apparent in both walls. The comparison at 1.50% drift reveals significantly lower compressive stress demands in CW3 overall due to the loss of load carrying capacity at this point in the loading history. Loss of confinement and crushing of the corner boundary element (BE) in CW3 results in the compressive stress being carried in the unconfined web and toe boundary element of the flange. While the compressive strain demand across the flange of CW1 remains largely uniform, the demand across the flange of CW3 is increasingly nonlinear as a result of the bi-directional loading.

A comparison of the vertical strain during weak axis loading with the ***web in compression*** for CW2 and CW3 is given in Fig. 17. The comparison at ~1.2% drift reveals relatively uniform vertical strain distribution across the web for both walls. The comparison at ~2.0% drift reveals a non-linear strain distribution across the web for both walls as result of the damage during bi-directional loading. CW2 indicates increased compressive stress to the left corner BE after the right corner BE experienced damage. Similarly, the loss of confinement and crushing of the corner boundary element on both sides of CW3 results in the demand being carried in the unconfined web between the boundary elements.

A comparison of the vertical strain during weak axis loading with the ***toe in compression*** for CW2 and CW3 is given in Fig. 18. The comparison at ~0.6% drift reveals relatively uniform vertical tensile strain distribution across the web for both walls; however, the flange reveals a large disparity in vertical compressive strain for CW3 due to the net tension loading and reduced overturning moment on the wall when acting as the tension pier of the coupled wall system. The comparison at 1.50% drift reveals a non-linear strain distribution across the web for both walls as result of the damage during bi-directional loading. The loss of bond and rupture of the web vertical reinforcement results in increased tensile

demand at the corner boundary elements. The reduced tensile in the web of CW3 between boundary elements indicates a significant loss of reinforcement consistent with the experimental observations.

There are several observations that can be made by comparing the aforementioned C-shaped wall tests to planar walls from Birely [24]. First, vertical strain fields indicate that for all C-shaped wall specimens, and particularly the bi-directionally loaded CW2 and CW3, the neutral axis depth when loaded in the strong-axis direction is considerably shallower than for the planar walls especially at higher drift levels. Second, the onset of substantial compressive straining occurs at a lower drift demand for the planar walls compared to the C-shaped wall ***web***. The differences in response between planar and C-shaped wall types can be attributed to the contribution of the flange in carrying compressive demand.

From the strain fields the following conclusions can be drawn for the C-shaped wall tests:

- The wall flanges contribute to carrying a rather significant portion of the compression demand thus reducing the demand on the wall web. As a result, the overall wall failure is tension-controlled rather than compression-controlled as observed in the planar walls;
- There is significant shear demand in the wall web, particularly in tension regions. With increasingly drift level, the shear demand in the flange becomes more significant along the base of the wall and in the boundary elements. Nonlinear strain distribution in the flanges appears to have a more rapid onset and greater magnitude in the bi-directionally loaded walls.
- The stiffness discontinuity in transitioning from a lightly-reinforced web to boundary element/flange results in a region of tensile straining (and high shear straining) along the edge of the compression boundary element.

5.3. Evaluation of response mechanisms based on deformation components

Another metric to evaluate the wall response is to compare the individual contributions of base slip, base rotation, shear deformation, and flexural deformation as a percentage of the total deformation throughout the loading history. The base rotation, base slip, first floor shear and first floor flexure components are calculated using displacements measured by the Nikon Metrology/Krypton system. The calculation follows the procedure of Birely [24]. At the second floor and third floor, shear and flexure components are calculated using linear displacement transducers located in vertical and diagonal orientations across the back face of the wall web. Deformation components were calculated from the transducers using the procedure of Massone and Wallace [25]. Fig. 19 displays the resulting deformation components of the walls up to 1% drift in the strong axis loading. The components of deformation during the initial phases of loading do not equal the total deformation due to instrumentation's limitations of measuring small displacements measured during elastic and cracking phases of the wall loading. Similarly, the components do not equal the total deformation after wall damage compromises the anchorage of the instruments into the wall which is observed in CW3 between the 0.5% and 1.0% drift level.

A general comparison of wall response reveals that shear and flexural deformations contribute nearly equally up to about 0.5% drift. During yielding of the reinforcement and up to the nominal strength at 0.75% drift, the flexural deformation of the first floor begins to dominate the response. Shear deformations remain relatively constant throughout the loading history tapering off only marginally during the formation of the plastic hinge in the first floor. In addition, the base slip and base rotation begin increasing around the nominal strength and have become a significant portion (20%) of the deformation at 1% drift.

When comparing the uni-directional test to the bi-directional tests, increased base slip and base rotation are observed in CW3. The tensile loading to the tension pier of the coupled wall system creates increased demand on the vertical reinforcement of the wall web leading to an earlier separation along the interface and higher contribution to the total deformation. Otherwise, no significant observations are apparent in the shear and flexural components up to the nominal strength. It is observed that beyond nominal at 1% drift the flexural deformation in the first floor is higher in the bi-directional test than the uni-directional test indicated the increased demand resulting from bi-directional loading. Further discussion of deformation components is available in Mock [20].

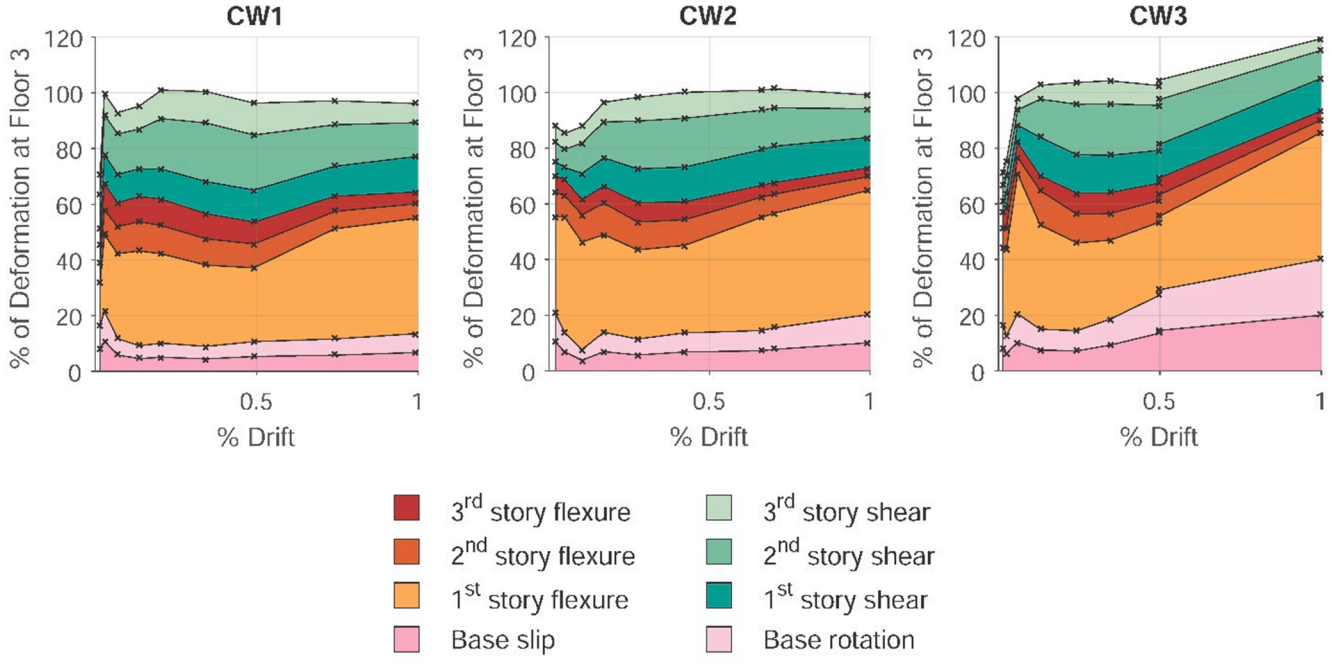

Fig. 19. Components of deformation for the C-shaped walls.

5.4. Evaluation of effective stiffness

In the seismic design or evaluation of reinforced concrete buildings, it is common for engineers to develop a linear elastic model that employs reduced, effective component stiffnesses. These stiffness values impact the calculated fundamental period, base-shear demand and lateral drift of a building as well as the demands on individual structural members. The effective stiffness expressions that appear in code, standard, and guideline documents for walls generally only address flexural stiffness and do not specifically consider the response of non-planar cross-sections. As an example, the ACI 318-11 [26] code recommends the flexural stiffness values of $0.35 - 0.70E_cI_g$ be utilized for walls based on level of cracking and indicates that the moment of inertia for non-planar cross-sections be calculated using an effective flange width. The recommendations from other code, standards, guideline, and research documents are summarized in Mock [20] and Mock et al. [27].

To investigate the appropriateness of existing effective stiffness recommendations for use with non-planar wall design, a study was conducted using experimental data from the C-shaped walls. The wall specimen was considered as a cantilevered Timoshenko beam with flexural stiffness (EI) and shear stiffness (GA) with a single point load applied at the effective wall height. The moment, shear, displacement, and average rotation of each floor were determined from the experimental data. Subsequently, the effective flexural (EI_{eff}) and shear (GA_{eff}) stiffness for each story level of the physical wall specimen and the average stiffness for the effective height of the ten-story prototype walls were computed, both considering and excluding base deformation. These effective stiffness values were determined for strong and weak-axis loading directions at the maximum and minimum peak of each displacement cycle. The effective stiffnesses were then plotted against effective drift level (drift at the effective height of the ten-story prototype wall based on the third-story drift of the C-shaped wall specimens). The approach for determining the effective stiffness values and effective drift level are further described in Birely [24], Mock [20], and Mock et al. [27].

Fig. 20 presents the effective stiffness values of each of the C-shaped specimens; these are average stiffnesses for the effective height of the prototype wall including rotation resulting from yield penetration of the longitudinal reinforcement. For comparison, recommendations for effective stiffness values from PEER/ATC-72-1 [28] and CSA A23.3 Code [29] as well as nonlinear effective stiffness models proposed by Brown [30] and Doepker [31] are also included. Each of the red circles on the C-shaped wall curves indicate the secant stiffness associated with onset of yielding for a particular direction of loading in the walls; Table 7 summarizes the drift and stiffness values for each of these points.

Table 7
Effective stiffness values for C-shaped walls at onset of yielding.

Wall	Yield drift	Effective stiffness	
		Flexural	Shear
CW1 - Strong	0.31%	0.28	0.19
CW2 - Strong	0.29%	0.29	0.17
CW3 - Strong	0.32%	0.27	0.16
CW2 - North	0.96%	0.29	0.07
CW2 - South	0.59%	0.26	0.08

Examination of flexural stiffness in Fig. 20(a) shows that the strong-axis response for each of the C-shaped walls is in close agreement with the non-linear models. The positive weak-axis (web in compression) response corresponds with these models up until 0.4% drift and diverges slightly thereafter. In contrast, the negative weak-axis (toes in compression) response is consistently higher than the non-linear models by $0.175–0.275EI_{eff}/E_cI_g$ for a majority of drift levels due to the variation in stiffness between the weak-axis directions after cracking that cannot be captured with an elastic section property. In addition, the shear span ratio varies significantly between the weak axis directions and strong axis which is not a variable of the non-linear stiffness models. Nevertheless, the average flexural stiffness at yield for all loading directions is approximately $0.28E_cI_g$ which is only slightly below the ATC-72 [28] yield definition of flexural stiffness.

In terms of shear stiffness, the average effective shear stiffness at yield was $0.17G_cA_g$ and $0.08G_cA_g$ for strong and weak-axis loading, respectively (Fig. 20(b)). For all drift levels, the strong-axis response of each wall shows a consistent shear stiffness response, with yield values only slightly above the ATC-72 [28] yield definition for effective shear stiffness. For weak-axis loading, the weak-axis/South direction is much stiffer than weak-axis/North loading at low drifts (<0.1%). However, beyond this drift level the weak-axis/North response tends to be stiffer than the strong-axis response, while the weak-axis/South is softer that the strong-axis response. This difference between the effective shear stiffness of the weak-axis (positive and negative) directions follows the trend seen with the flexural stiffness. For the strong-axis direction, bi-directional loading does not have an impact on either flexural or shear effective stiffness values. Further discussion of effective stiffness of walls is available in Mock [20].

6. Conclusions

Three large-scale C-shaped walls were tested at the NSEL UIUC MUST-SIM facility as part of a larger study examining the seismic performance of structural concrete walls. The nominally identical C-shaped

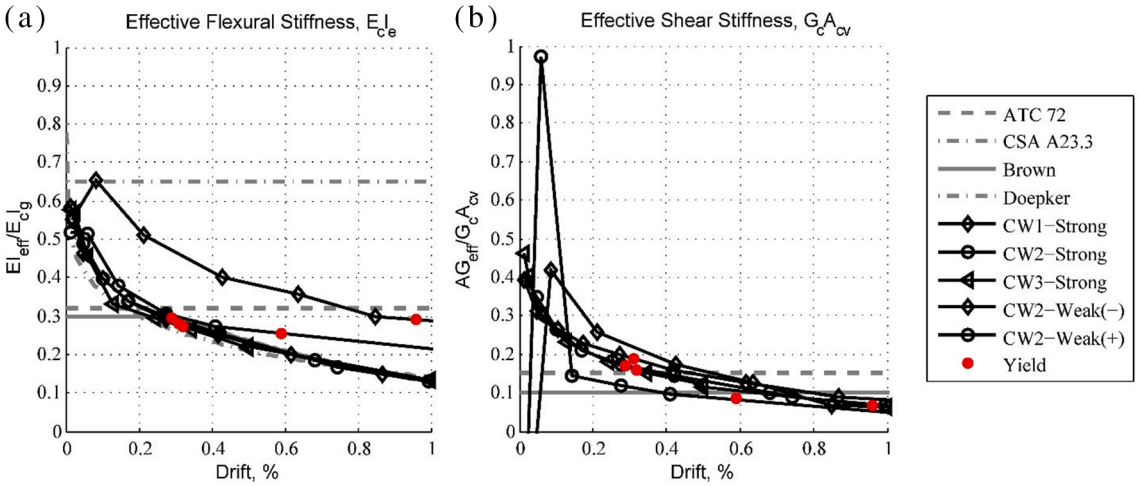

Fig. 20. Effective stiffness values for C-shaped walls compared to code and research recommendations. (a) Flexural and (b) shear stiffness.

wall specimens were designed to reflect modern wall details found in current industry practice and code requirements. The one-third scale models were used to simulate the lower three stories of a ten-story prototype wall and were subjected to a quasi-static lateral loading and axial loading. The tests investigated the impact of: (1) bi-directional lateral loading and (2) variable axial loading that occurs in wall piers in a coupled core wall system. To more fully understand the earthquake performance of C-shaped walls, test results including global load-deformation, damage, as well as localized and full-field deformation data were analyzed. The following summarizes the observations and conclusions of this work:

1. The strong-axis drift capacity of the uni-directionally loaded wall was approximately 1.75% and for the bi-directionally loaded walls it was at or slightly beyond 1.5%. The bi-directionally loaded walls were able to sustain weak-axis drift demands in excess of 1.5%.
2. For strong-axis bending, both uni- and bi-directionally loaded walls had essentially the same flexural strength (within 91–95% of nominal flexural strength calculated per ACI 318-19 [1] and were able to maintain a similar load-deformation response until 0.75% drift.
3. The damage progression in all walls was similar. Yielding and fracture of a majority of No. 2 bars in the wall web led to significant sliding of wall web at wall-foundation interface; this sliding was resisted by dowel action (shearing) of longitudinal reinforcement in the corner boundary elements and out-of-plane response of the wall flanges. Ultimately, the boundary elements sustained crushing of confined concrete and buckling followed by rupture of longitudinal reinforcement which led to significant loss in lateral-load carrying capacity of the wall.
4. For each of the C-shaped walls, strain gauge measurements indicate that compression yielding is limited and typically only occurs after repeated cycles of loading that has already resulted in tension strain hardening. This is distinct from planar walls tested by Lowes et al [5] where researchers noted that compression yielding preceded tension yielding.
5. Strain fields calculated from full-field measurements indicate that the walls' neutral axis is rather shallow. The wall flanges contribute to carrying a significant portion of the compression demand, such that the region and magnitude of compression demand on the wall web is limited. Also, shear straining is significant along diagonal bands in the wall web, at the base of the flanges, and at the web-boundary element transition at the wall corners.
6. Flexural deformation at the first floor dominates the response of the uni- and bi-directionally loaded C-shaped wall specimens; however, base slip and rotation become substantially more significant for the bi-directionally loaded CW3 wall as drift demands increase.
7. Uni- and bi-directionally loaded walls exhibit nearly identical effective flexural and shear stiffnesses up to 1% drift; moreover, yield values are reasonably consistent with ATC-72 [28].

CRediT authorship contribution statement

Anahid A. Behrouzi: Investigation, Formal analysis, Data curation, Visualization, Writing - original draft, Writing - review & editing. **Andrew W. Mock:** Software, Investigation, Formal analysis, Data curation, Visualization, Writing - original draft. **Dawn E. Lehman:** Conceptualization, Funding acquisition, Supervision, Writing - original draft, Writing - review & editing. **Laura N. Lowes:** Conceptualization, Funding acquisition, Supervision, Writing - original draft. **Daniel A. Kuchma:** Conceptualization, Funding acquisition, Project administration, Writing - original draft.

Declaration of Competing Interest

The authors declare that they have no known competing financial interests or personal relationships that could have appeared to influence the work reported in this paper.

Acknowledgements

The authors would like to acknowledge the contributions of prior graduate students Christopher Hart and Ken Marley of the University of Illinois, and Anna Birely of the University of Washington. The authors would also like to acknowledge the contributions of Professor Emeritus Neil Hawkins, University of Illinois; Ron Klemencic and John Hooper of Magnusson Klemencic Associates, Seattle; Andrew Taylor of KPFF, Seattle and Joe Maffei of Rutherford & Chekene, San Francisco in advising the practical aspects of the research program.

The research presented herein was funded by the Charles Pankow Foundation, McLean, VA via Grant # 03-09 and the National Science Foundation through the Network for Earthquake Engineering Simulation Research Program, Grants # CMS-0421577 and CMMI-0927178, Joy Pauschke, program manager. Any opinions, findings, and conclusions or recommendations expressed in this material are those of the authors and do not necessarily reflect the views of the Charles Pankow Foundation or the National Science Foundation.

Appendix A. Supplementary material

Supplementary data to this article can be found online at https://doi.org/10.1016/j.engstruct.2020.111289.

References

[1] ACI 318-19. Building code requirements for structural concrete (ACI 318-19) and commentary (ACI 318 R-19). American Concrete Institute; 2014.
[2] Beyer K, Dazio A, Priestly MJN. Quasi-static cyclic tests of two u-shaped reinforced concrete walls. J Earthquake Eng 2008;12(7):1023–53.
[3] Constantin R-T. Seismic behaviour and analysis of u-shaped RC walls. PhD thesis, Ecole Polytechnique Federale de Lausanne (EPFL); 2016.
[4] Sarkisian M, Mathias NJ, Long E. Seismic design and detailing of compound shear wall plan configurations. Council on Tall Buildings and Urban Habitat (CTBUH) Research Paper 2003.
[5] Lowes LN, Lehman DE, Birely AC, Kuchma DA, Marley KP, Hart CR. Earthquake response of slender planar concrete walls with modern detailing. Eng Struct 2012;43:31–47.
[6] Lehman DE, Turgeon JA, Birely AC, Hart CR, Marley KP, Kuchma DA, et al. Seismic behavior of a modern concrete coupled wall. J Struct Eng, ASCE 2013;139(8):1371–81.
[7] [dataset] Birely A, Mock AW, Behrouzi AA, Kuchma DA, Lehman DE, Lowes LN. Seismic behavior of modern reinforced concrete c-shaped walls (Specimen UW6), Network for Earthquake Engineering Simulation (distributor), Dataset, doi: 10.4231/D3C24QP0D; 2014. <https://www.designsafe-ci.org/data /browser/public/nees.public/NEES-2005-0104.groups>.
[8] [dataset] Behrouzi AA, Mock AW, Birely A, Kuchma DA, Lehman DE, Lowes LN. Seismic behavior of modern reinforced concrete c-shaped walls (Specimen UW7). Network for Earthquake Engineering Simulation (distributor), Dataset, doi: 10.4231/D37D2Q79C; 2014. <https://www.designsafe-ci.org/data /browser/public/nees.public/NEES-2005-0104.groups>.
[9] [dataset] Mock AW, Behrouzi AA, Birely A, Kuchma DA, Lehman DE, Lowes LN. Seismic behavior of modern reinforced concrete c-shaped walls (Specimen UW8), Network for Earthquake Engineering Simulation (distributor), Dataset, doi: 10.4231/D33N20F5M; 2014. <https://www.designsafe-ci.org/data /browser/public/nees.public/NEES-2005-0104.groups>.
[10] Sittipunt C, Wood SL. Finite element analysis of reinforced concrete shear walls. Technical report, University of Illinois at Urbana-Champaign; 1993.
[11] Ile N, Reynouard JM. Behaviour of u-shaped walls subjected to uniaxial and biaxial cyclic lateral loading. J Earthquake Eng 2005;9(1):67–94.
[12] Lowes LN, Lehman DE, Kuchma DA, Behrouzi AA, Mock AW. Summary of large scale c-shaped reinforced concrete wall tests. Report to the Charles Pankow Foundation on Grant; 2015. <https://www.pankowfoundation.org/grants?ID=28&Grant_=03-09>.
[13] ACI 318-08. Building code requirements for structural concrete (ACI 318-08) and commentary (ACI 318 R-08). American Concrete Institute; 2008.
[14] Mohr DS. Nonlinear analysis and performance based design methods for reinforced concrete coupled shear walls. MS thesis. University of Washington; 2007.
[15] Turgeon JA. The seismic performance of coupled reinforced concrete walls. MS thesis. University of Washington; 2011.
[16] ASCE/SEI 7-10. Minimum design loads for buildings and other structures. NY: American Society of Civil Engineering; 2010.
[17] Brown PC, Ji J, Oyen P, Sterns A, Lehman DE, Lowes LN, et al. Investigation of the seismic behavior and analysis of reinforced concrete structural walls. Proceedings of 100th Anniversary Earthquake Conference. 2006.

[18] Harries KA. Ductility and deformability of coupling beams in reinforced concrete coupled walls. Earthquake Spectra 2001;17(3):457–78.
[19] Behrouzi AA. Impact of cross section, web reinforcement and load history on the seismic performance of slender concrete walls. PhD thesis. University of Illinois at Urbana-Champaign; 2016.
[20] Mock AW. Performance of c-shaped structural concrete walls subjected to bi-directional loading. PhD thesis. University of Illinois at Urbana-Champaign; 2018.
[21] Ozselcuk AR. Experimental and analytical studies of coupled wall structures. PhD thesis. Berkeley: University of California; 1989.
[22] Lequesne RD, Wight JK, Parra-Montesinos GJ. Seismic detailing and behavior of coupled-wall systems with high-performance fiber-reinforced concrete. Proceedings of 9th US National and 10th Canadian Conference on Earthquake Engineering, Earthquake Engineering Research Institute and the Canadian Association for Earthquake Engineering; 2010.
[23] Hoehler MS, Stanton JF. Simple phenomenological model for reinforcing steel under arbitrary load. J Struct Div, ASCE 2006;132(7):1061–9.
[24] Birely A. Seismic performance of slender reinforced concrete structural walls. PhD thesis. University of Washington; 2012.
[25] Massone LM, Wallace JW. Load-deformation responses of slender reinforced concrete walls. ACI Struct J 2004;101(1):103–13.
[26] ACI 318-11. Building code requirements for structural concrete (ACI 318-11) and commentary (ACI 318 R-11). American Concrete Institute; 2011.
[27] Mock AW, Behrouzi AA, Lowes LN, Lehman DE, Kuchma DA. Recommendation for effective stiffness expression for elastic analysis of concrete walls. Report to the Charles Pankow Foundation on Grant; 2015. < https://www.pankowfoundation.org/grants?ID=28&Grant_=03-09>.
[28] Moehle JP, Mahin S, Bozorgnia Y. Modeling and acceptance criteria for seismic design and analysis of tall buildings (PEER/ATC-72-1). Applied Technology Council 2010.
[29] CSA A23.3-04. Design of concrete structures (CSA A23.3-04). Standards Council of Canada; 2004 and reaffirmed 2010.
[30] Brown PC. Probabilistic earthquake damage prediction for reinforced concrete building components. MS thesis. University of Washington; 2008.
[31] Doepker BD. Evaluation of practical methods for the evaluation of concrete walls. MS thesis. University of Washington; 2008.